

**Field Ionization and Field Emission  
with Intense, Single-cycle THz Pulses  
Need to replace with my own title**

by

© Yunxiao Wang

A thesis submitted to the  
School of Graduate Studies  
in partial fulfilment of the  
requirements for the degree of  
Anqing, Anhui, China

B.S. in Physics University of Science and Technology of China May 2009

Memorial University of Newfoundland

Doctor of Philosophy

St. John's

Newfoundland

Department of Physics August, 2016

## Abstract

Nuclear-polarized  $^3\text{He}$  targets have been widely used in electron-scattering experiments in Thomas Jefferson National Accelerator Facility (JLAB) since mid 1990s. It is of great importance to produce large amounts of  $^3\text{He}$  gas with high polarization.

The latest experiments run in JLAB prior to the 12GeV upgrade have been using cells polarized with Spin-Exchange Optical Pumping (SEOP). These cells were made of the GE180 glass and use a two-chambered design. The top chamber, known as the pumping chamber, is where  $^3\text{He}$  is polarized through SEOP. The bottom chamber, known as the target chamber, is where electron scattering occurs. Great effort has been made in our lab to develop this generation of cells. Alkali-hybrid SEOP together with narrowband laser diode arrays have increased the  $^3\text{He}$  polarization from 37% to 65%. Among other things, we also carefully studied an additional spin relaxation mechanism that limits the maximum achievable  $^3\text{He}$  polarization.

The 12GeV upgrade makes the future experiments much more demanding in terms of target cell performance. One challenge it brings is the high relaxation due to electron beam. We have designed and tested a new style cell that uses convection instead of diffusion to increase the rate at which the polarization in the target chamber is being replenished by gas from pumping chamber. We have obtained over 50% polarization with controllable convection speed so far.

An additional problem that comes with higher beam current is that the glass end windows of traditional design are not likely to survive the experiments. Our group started exploring the option of using metal end windows from a decade ago. The first problem to solve is to find out the correct material and the proper technique

to incorporate metal without introducing significant spin relaxation and still being able to hold high pressure gas (12 atm) inside. This is a brand new technique that may have a profound impact of future cell designs once fully developed. Although no metal end windows have been tested so far, multiple glass cells with different kinds metal tubes (much larger in area compared to the end windows that will be used in JLAB experiments) attached were examined and were enough to convince us the extra spin relaxation is not likely to cause significant problems. The metals tubes were connected to Pyrex glass with knife-edge (housekeeper) seals and stayed intact through high pressure tests. After exploring options such as pure copper, gold coated copper, titanium, stainless steel, gold coated titanium, we have established that electroplating gold on copper substrate yields the best result so far. Further tests are planned before attaching metal end windows to GE180 glass and using them in electron-scattering experiments.

## Acknowledgements

Put your acknowledgements here...

*“Intellectual and practical assistance, advice, encouragement and sources of monetary support should be acknowledged. It is appropriate to acknowledge the prior publication of any material included in the thesis either in this section or in the introductory chapter of the thesis.”*

— MUN School of Graduate Studies

# Contents

<b>Abstract</b>	<b>ii</b>
<b>Acknowledgements</b>	<b>iv</b>
<b>List of Tables</b>	<b>viii</b>
<b>List of Figures</b>	<b>x</b>
<b>1 Spin-Exchange Optical Pumping</b>	<b>1</b>
1.1 Overview . . . . .	1
1.2 Optical pumping . . . . .	2
1.2.1 Rb for SEOP . . . . .	2
1.2.2 Vapor Pressure Curves . . . . .	3
1.2.3 Energy Levels of Alkali Metal in External Magnetic Field . . .	3
1.2.4 Optical Pumping Process Overview . . . . .	5
1.2.5 Optical Pumping Rate . . . . .	7
1.2.6 Polarization Time Evolution . . . . .	11
1.2.7 Rb Spin Destruction Rate . . . . .	13
1.3 Spin Exchange . . . . .	14

1.3.1	Spin-Dependent Interactions . . . . .	14
1.3.2	Spin Exchange Rate . . . . .	18
1.4	$^3\text{He}$ Spinup and Relaxation . . . . .	19
1.5	X Factor . . . . .	21
<b>2</b>	<b><math>^3\text{He}</math> Polarimetry</b>	<b>22</b>
2.1	Overview . . . . .	22
2.2	Adiabatic Fast Passage . . . . .	23
2.2.1	Nuclear Magnetic Resonance . . . . .	23
2.2.2	The Rotating Coordinate System . . . . .	24
2.2.2.1	Classical Formulation . . . . .	24
2.2.2.2	Quantum Mechanical Formulation . . . . .	25
2.2.3	Adiabatic Fast Passage . . . . .	26
2.2.4	AFP Loss . . . . .	31
2.3	Electron Paramagnetic Resonance . . . . .	34
2.3.1	Overview . . . . .	34
2.3.2	The Breit-Rabi Equation . . . . .	35
2.3.3	Shift of Zeeman Frequency . . . . .	36
2.3.4	Experimental Methods . . . . .	38
2.3.4.1	Overview . . . . .	38
2.3.4.2	Locating Zeeman Transition Frequency . . . . .	39
2.3.4.3	EPR Spin Flip Process . . . . .	41
2.4	Pulsed Nuclear Magnetic Resonance . . . . .	44
2.4.1	The Rotating Coordinate System . . . . .	44

2.4.2	Free Induction Decay . . . . .	45
2.4.3	Experimental Methods . . . . .	47
<b>3</b>	<b>Development of Hybrid Targets</b>	<b>52</b>
3.1	Overview . . . . .	52
3.2	Development of Targets without Convection . . . . .	53
3.2.1	Experimental Methods . . . . .	55
3.2.1.1	The $^3\text{He}$ Targets . . . . .	55
3.2.1.2	Target Cell Polarization Dynamics . . . . .	58
3.2.1.3	Initial Spinup . . . . .	63
3.2.1.4	The K- $^3\text{He}$ Spin-Exchange Rate Constant . . . . .	67
3.2.1.5	The X Factor . . . . .	70
	<b>Bibliography</b>	<b>79</b>
<b>A</b>	<b>Appendix title</b>	<b>81</b>

# List of Tables

1.1	Pressure broadening of Rb D <sub>1</sub> lines by <sup>3</sup> He, <sup>4</sup> He and N <sub>2</sub> . The broadening and shifting density coefficients are listed. The 4th and 6th columns are the temperature dependence for He and N <sub>2</sub> , respectively. All coefficients are given for 353 K, values for different temperatures can be calculated with the temperature dependence. . . . .	8
3.1	The table contains the names, total and pumping chamber volumes, fill densities and target chamber lengths of the 24 target cells. The fill densities are the average of the results from gas system measurements and pressure broadening measurements. . . . .	59



3.2	Cell Performance for three sets of experiments: saGDH (top), GEN (middle), and Transversity & $d_2^n$ (bottom). Within each experiment grouping, data is grouped by type of laser used (B = Broadband, N = Narrowband). $I_0$ is the nominal incident laser intensity at the center of the pumping chamber. $T_{pc}^{set}$ is the oven set temperature. $P_{pc}^\infty$ is the equilibrium polarization in the pumping chamber and $\Gamma_s$ is the slow time constant extracted from the five parameter fit to the polarization build up curve. $\Gamma_c$ is the cell-averaged room temperature spin relaxation rate. $\langle P_A \rangle / P_A^l$ is the volume averaged to line averaged alkali polarizaiton ratio determined from the optical pumping simulation. $P_A^l$ is the measured line averaged alkali polarization. $D_{fr} \& D_{pb}$ are the K to Rb density ratios determined from Faraday rotation and pressure broadening measurements. $[Rb]_{fr}$ is the Rb number density measured from Faraday rotation. $\Delta T_{He}$ is the temperature of Rb inferred from the number density relative to the oven set temperature. $\Delta T_{He}$ is the temperature of $^3\text{He}$ inferred from temperature tests relative to the oven set temperature. X is the best combined value for the X-factor. * indicates X was measured using only spinup, alkali polarization, and Faraday rotation data. $^\dagger$ indicates X was also measured using the early-time behavior of the spinup. . . . .	72
3.3	Shown are the values of the X factor at the indicated over set temperatures. The last column is a weighted average of results from either the first two methods or all four methods. A $^\dagger$ indicates combined values computed with all 4 methods. . . . .	78

# List of Figures

1.1	Rb And K Number Density Curves . . . . .	4
1.2	Level Diagram of $^{87}\text{Rb}$ . The splittings are not to scale. Adapted from Dolph's PhD thesis. . . . .	6
1.3	The interaction of alkali-metal atoms with left-circularly ( $\sigma^+$ ) polarized light. (from Ref. [10]) . . . . .	7
1.4	Absorption cross section for Rb $D_1$ line in the presence of three different densities of $^3\text{He}$ . (from Ref. [6]) . . . . .	9
1.5	The shift and the broadening due to presence of $^3\text{He}$ for Rb $D_1$ and $D_2$ lines. (from Ref. [6]) . . . . .	10
1.6	A. Formation and breakup of alkali-metal/noble-gas van der Waals molecule. B. Binary collision between an alkali-metal atom and a noble-gas atom. (from Ref. [10]) . . . . .	16
1.7	Strengths of various spin-dependent interactions as functions of separation(from Ref. [10]) . . . . .	17
2.1	EPR (left) and AFP (right) setup. Adapted from Dolph's PhD thesis. . . . .	27

2.2	Effective field in the rotating frame during an Adiabatic Fast Passage measurement. The $^3\text{He}$ spins follow the direction of the effective field. $B_1$ is exaggerated to show different components of effective field clearly. . . . .	30
2.3	A typical AFP signal. y axis is in arbitrary unit. . . . .	31
2.4	Fractional AFP loss (single flip) as a function of field gradient. . . . .	33
2.5	A typical FM sweep on a hybrid cell. The central region between the minimum and maximum is fitted to a line. The zero crossing point corresponds to the Zeeman transition frequency. . . . .	41
2.6	The same P.I. circuit that was first used by Romalis in our lab. The drawing was then corrected by Peter Dolph.[1] . . . .	42
2.7	An EPR measurement for a hybrid cell at 235°C. . . . .	43
2.8	PNMR setup. . . . .	48
2.9	A PNMR signal taken with gold coated test cell. . . . .	50
3.1	Shown are two figures of merit (FOM) for targets built for the indicated experiments. The circles (left axis) indicate the number of spins being polarized per second weighted by the square of polarization. The bars (right axis) represent the luminosity weighted by the square of polarization. While the first FOM is an indication of the potential of the polarization technique, the second FOM indicates performance achieved during an experiment. The actual cells used to formulate the FOMs are not necessarily the same. . . . .	56

3.2	<b>A target cell. The dimensions of different parts of the cell are not to scale.</b>	57
3.3	(a) Shown is a spinup of the target Brady. The spinup data has been fit with a 3-parameter and a 5-parameter formalism. (b) The residuals of the two fits. The error for 3-parameter fit is larger because it does not account for diffusion between two chambers. Adopted from [?].	60
3.4	<b><math>^3\text{He}</math> polarization as a function of time for both the pumping chamber and the target chamber. The top curve is the pumping chamber and the bottom curve is the target chamber. Data was taken at a fast pace so there would be enough points to demonstrate the initial behavior.</b>	64
3.5	Plotted is the ratio $m_{pc}^F/m_{pc}^s$ for eight separate measurements. The numbers above the cell names are the oven set temperatures at which the measurements were made.	70
3.6	The cell-averaged spin-exchange rate $\langle\gamma_{se}\rangle$ is calculated using data from Faraday rotation and the spin-exchange constants $k_{se}^{Rb}$ and $k_{se}^K$ . The three linear fits shown here are constrained to go through zero. The errors quoted in values of X factor include the uncertainty in our determination of $k_{se}^K$ .	75

# Chapter 1

## Spin-Exchange Optical Pumping

### 1.1 Overview

Spin-polarized noble gases have been widely used for various purposes. In JLAB, polarized  $^3\text{He}$  is used as target for electron-scattering experiments. This is because a  $^3\text{He}$  nucleus has a pair of protons with paired spins and a single neutron that contributes the most of the nuclear spin. In MRI, polarized  $^3\text{He}$  has seen uses such as detecting structural damage in the lungs.

There are generally two ways of polarizing  $^3\text{He}$ : Metastability-Exchange Optical Pumping (MEOP) and Spin-Exchange Optical Pumping (SEOP). Our group focuses on SEOP as MEOP polarizes gas at relatively low pressure ( $\sim 1$  torr), thus further compression is required to produce target cells of several atms that meet the need of JLab experiments.

In SEOP, alkali metal is polarized by circularly polarized laser tuned to the D1 transition of the particular alkali species used.  $^3\text{He}$  obtains polarization from alkali

metal through spin exchange process. With the combination of hybrid alkali mixtures (typically Rb and K) and spectrally narrowed lasers, more than 70% polarizations have been produced.

## 1.2 Optical pumping

### 1.2.1 Rb for SEOP

In optical pumping, Rb is often the alkali metal chosen to be optically pumped by circularly polarized laser light. The angular momentum of a polarized photon is transferred to the valence electron of Rb atom. In the case of hybrid mixture of Rb/K, Rb is still the alkali metal that is directly pumped by laser light while K serves as an efficient medium to transfer the polarization from Rb to  $^3\text{He}$ . Because the spin destruction rates are much lower for lighter alkali metals, K- $^3\text{He}$  spin-exchange process is a lot more efficient than that of Rb- $^3\text{He}$ . However, it is still much easier to optically pump Rb and transfer the polarization to  $^3\text{He}$  through K, mainly for Rb's low melting point, the relative ease of acquiring laser at the Rb D1 line wavelength and the wide separation between D1 (794.7nm) and D2 line (780nm).

The Rb melting point is at 39.5°C, so it's easy to achieve enough Rb vapor without having to drive the oven temperature too high. In our lab, depending on if the cell contains pure Rb or Rb/K mixture, the oven temperature can be between 85°C to as high as 255°C. Perhaps the most used oven temperature for hybrid is 235°C which has empirically been a good temperature to produce Rb/K mixture vapor, while 85°C is enough for pure Rb.

### 1.2.2 Vapor Pressure Curves

When the alkali metal is heated to above its melting point, a small amount of alkali metal atoms evaporate. The equilibrium vapor pressure is temperature dependent:

$$P = 10^{5.006+\alpha+\beta/T} Pa \quad (1.1)$$

where  $\alpha$  and  $\beta$  are listed in Table 1.2.2.

	Patassium	Rubidim
$\alpha$	4.402	4.312
$\beta$	-4453	-4040

Thus the number density is

$$[A] = \frac{10^{5.006+\alpha+\beta/T}}{k_B T} \quad (1.2)$$

The number density curves of pure Rb and K vapor are shown in Fig. 1.1.

### 1.2.3 Energy Levels of Alkali Metal in External Magnetic Field

The Hamiltonian for ground state (L=0) alkali metal atoms in external magnetic field is:

$$\mathbf{H} = A\mathbf{I} \cdot \mathbf{S} + g_e\mu_B S_z B_z + g_N\mu_N I_z B_z \quad (1.3)$$

The first term  $A\mathbf{I} \cdot \mathbf{S}$  describes the coupling of the nuclear spin  $\mathbf{I}$  with the electron spin  $\mathbf{S}$  and is key to spin exchange, where A is the isotropic magnetic-dipole coupling

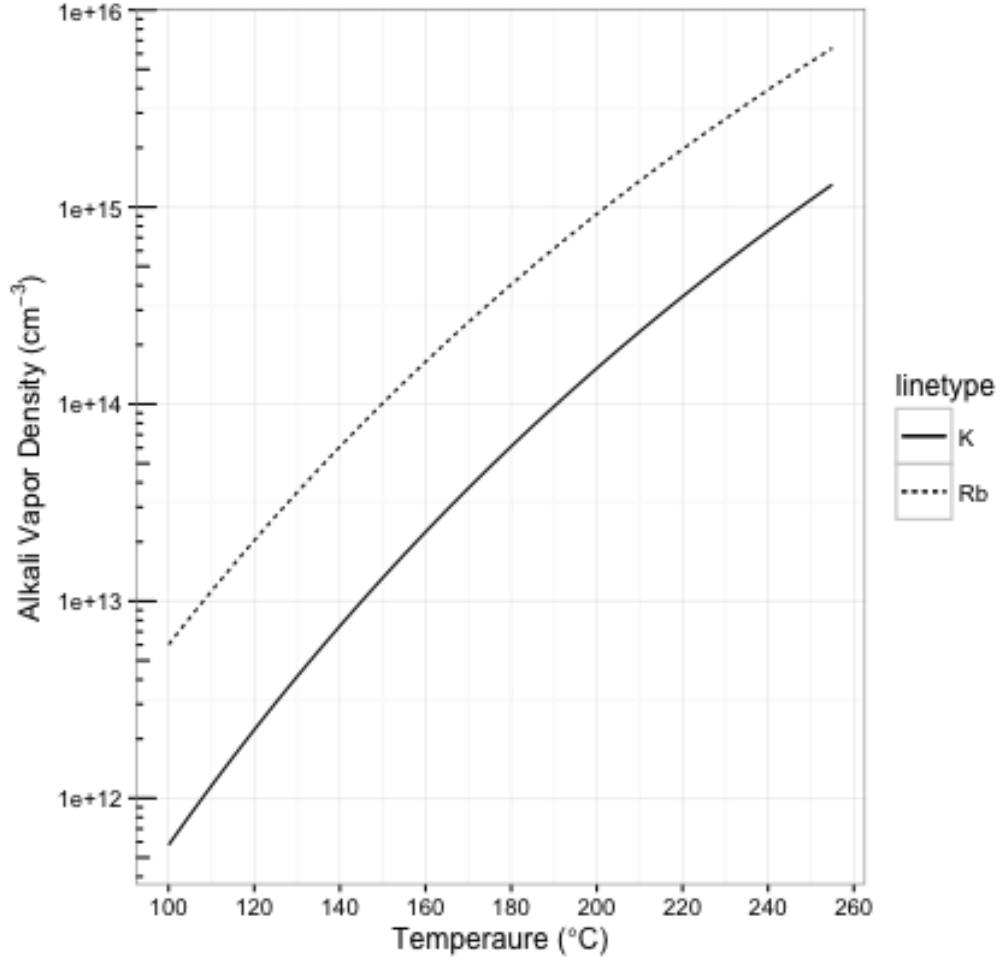


**Figure 1.1: Rb And K Number Density Curves**

coefficient. The resulting energy levels from the first term are referred to as hyperfine structure. The second and third terms describe the Zeeman splitting due to the presence of a weak external magnetic field.  $\mu_B = 9.274 \times 10^{-24} J/T$  and  $\mu_N = 5.051 \times 10^{-27} J/T$  are the Bohr and nuclear magnetons.  $g_e \approx 2$  and  $g_N \approx 5.59$  are the electronic and nuclear Lande g-factors.

The linear relationship between energy levels and magnetic field only holds for weak magnetic fields which applies to our lab where  $\sim 13$  Gauss is used most of the



time. When the Zeeman splitting grows comparable to the hyperfine energy difference one would have to take into account the quantum mixing of the states, the result is described by Breit-Rabi Formula. With  $\sim 13$  Gauss, the hyperfine term dominates the total Hamiltonian. The energy levels of  $^{87}\text{Rb}$  are shown in Fig. 1.2.

### 1.2.4 Optical Pumping Process Overview

For simplicity, the following discussion will ignore the nuclear spins for now. The inclusion of nuclear spins will increase the number of energy states but the optical pumping mechanism remains the same. In our typical setup, circularly polarized laser light is tuned to the D1 line of Rb and excites valence electrons of Rb from  $5S_{1/2}$  state to  $5P_{1/2}$  state as shown in Fig. 1.3 ( $2S_{1/2}$  and  $2P_{1/2}$  states are used in the simple model described by the figure below).

Left-circularly polarized light is assumed in the figure, but either circular polarization works the same. Conservation of angular momentum requires  $\Delta m = +1$  as the figure shows. Through collisions with other Rb atoms, excited electrons will mix and evenly distribute on the two  $2P_{1/2}$  states. Electrons then decay to the two ground states with equal probabilities. The selection rule for the decay process is  $\Delta m = 0$  or  $\pm 1$ . Even though both ground states receive electrons from the decay, only the  $m = -1/2$  state absorbs the circular polarized photons and is being depleted, so atoms are in effect pumped to the  $m = +1/2$  state. When we consider Rb with nuclear spins, both  $5S_{1/2}$  and  $5P_{1/2}$  states are split into more energy levels, but the net effect is still that the ground state with highest  $m$  accumulate atoms over time.

When the excited electrons decay back to the ground state, they emit unpolarized

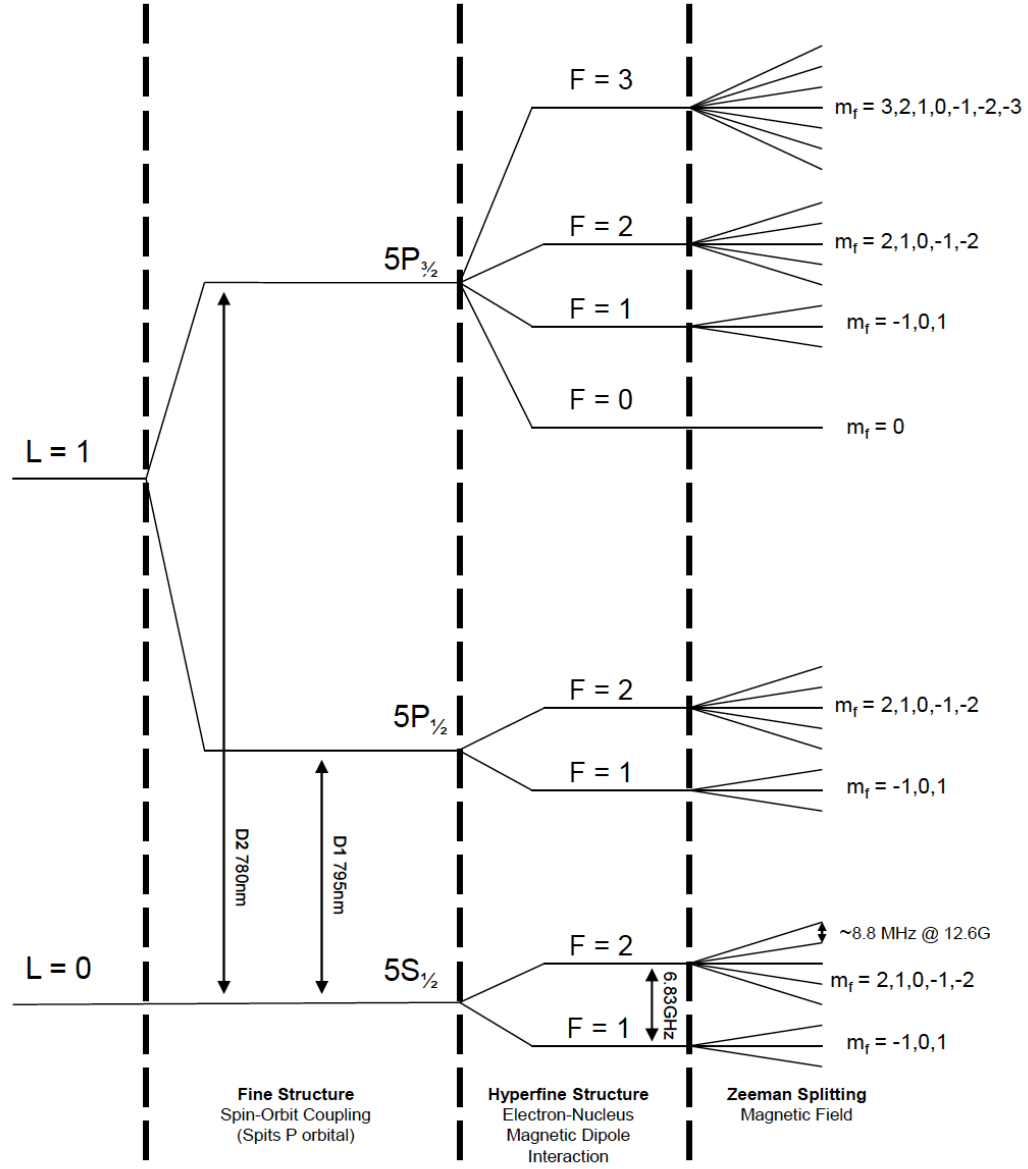


Figure 1.2: Level Diagram of  $^{87}\text{Rb}$ . The splittings are not to scale. Adapted from Dolph's PhD thesis.

photons with angular momentum in random directions which can depolarize the gas. A small amount of  $\text{N}_2$  gas is added into the cell (typically around 0.1 Amagats) to non-radiatively quench the excited electrons as  $\text{N}_2$  molecules can absorb the released

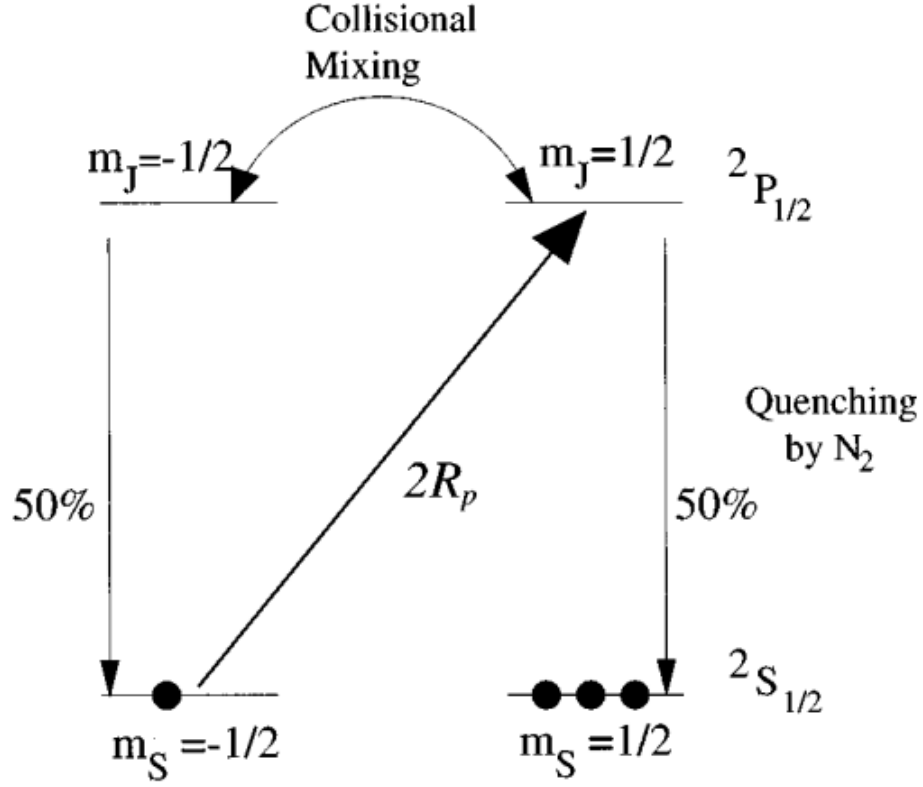


Figure 1.3: The interaction of alkali-metal atoms with left-circularly ( $\sigma^+$ ) polarized light. (from Ref. [10])

energy of spontaneous decays into their rotational and vibrational modes of oscillation. With an appropriate amount of N<sub>2</sub>, the photon-emitting decays can be reduced to less than 5%.

### 1.2.5 Optical Pumping Rate

The optical pumping rate at position  $\vec{r}$  can be described by

**Table 1.1:** Pressure broadening of Rb D<sub>1</sub> lines by <sup>3</sup>He, <sup>4</sup>He and N<sub>2</sub>. The broadening and shifting density coefficients are listed. The 4th and 6th columns are the temperature dependence for He and N<sub>2</sub>, respectively. All coefficients are given for 353 K, values for different temperatures can be calculated with the temperature dependence.

	<sup>4</sup> He	<sup>3</sup> He	Temp. depen.	N <sub>2</sub>	Temp. depen.
D <sub>1</sub> full width (GHz/amg)	18.0±0.2	18.7±0.3	T <sup>0.05±0.05</sup>	17.8±0.3	T <sup>0.3</sup>
D <sub>1</sub> line shift (GHz/amg)	4.3±0.1	5.64±0.15	T <sup>1.1±0.1</sup>	-8.25±0.15	T <sup>0.3</sup>

$$R = \int \Phi(\nu, \vec{r}) \sigma(\nu) d\nu \quad (1.4)$$

where  $\Phi(\nu, \vec{r})$  is the position dependent photon spectral flux density and  $\sigma(\nu)$  is the photon absorption cross section. The cross section has a natural Lorentzian lineshape which is broadened by Doppler effect and pressure broadening. The pressure broadening effect dominates the lineshape as our cells normally have densities well above one amagat. The collisions of Rb with <sup>3</sup>He and N<sub>2</sub> cause the broadening as well as a slight shift of the D<sub>1</sub> line. The coefficients of pressure broadening for <sup>3</sup>He, <sup>4</sup>He and N<sub>2</sub> are listed in Table 1.1, and can be used to calculate the broadened line width and the shifted line center.

$\sigma(\nu)$  follows the sum rule:

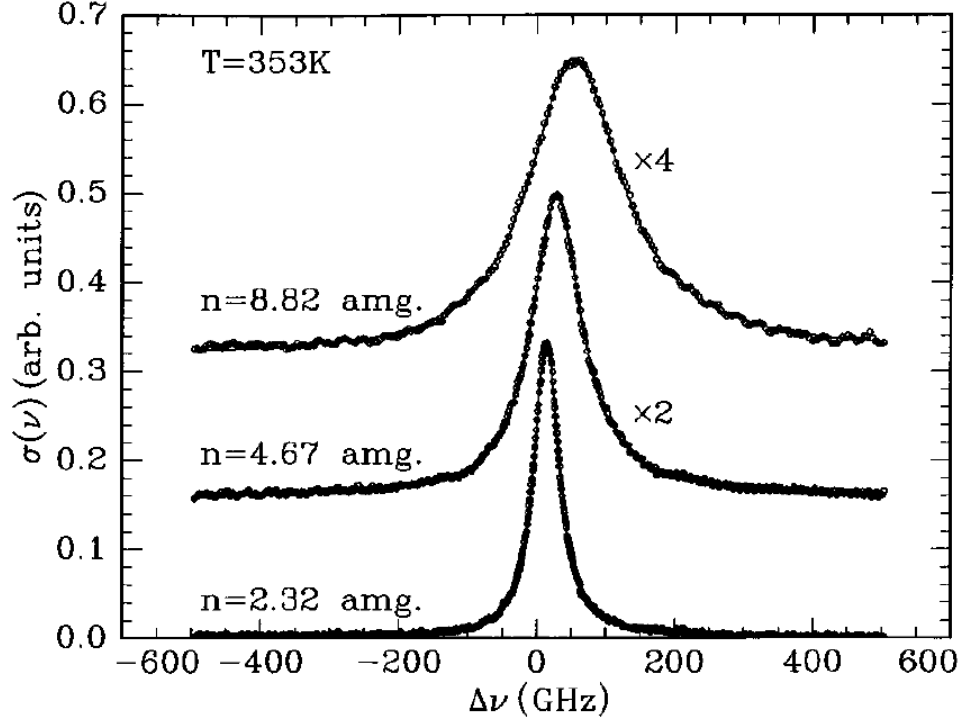


Figure 1.4: Absorption cross section for Rb  $D_1$  line in the presence of three different densities of  $^3\text{He}$ . (from Ref. [6])

$$\int \sigma(\nu) d\nu = \pi r_0 c f \quad (1.5)$$

where  $r_0 = 2.82 \times 10^{-13}$  cm is the classical electron radius and  $f=0.337$  is the transition oscillator strength. Thus the photon absorption cross section can be described by Lorentzian lineshape:

$$\sigma(\nu) = f r_e c \frac{\frac{\Gamma_A}{2}}{(\nu - \nu_0)^2 + (\frac{\Gamma_A}{2})^2} \quad (1.6)$$

where  $\Gamma_A$  is the pressure dependent FWHM,  $\Gamma_A \approx 0.04 \text{ nm/amg} \cdot [^3\text{He}]$ . At the front of the cell, the photon spectral flux density is the product of a Gaussian spatial

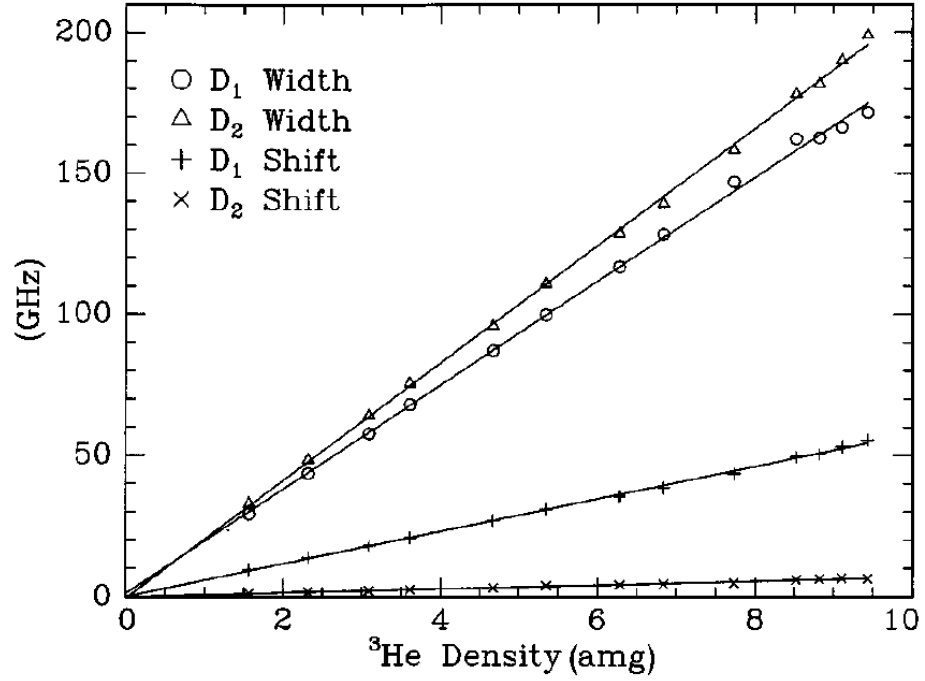


Figure 1.5: The shift and the broadening due to presence of  $^3\text{He}$  for Rb  $D_1$  and  $D_2$  lines. (from Ref. [6])

distribution and a Gaussian spectrum.

$$\phi(\nu, \vec{r}) = \phi_0(\vec{r})G(\nu) \quad (1.7a)$$

$$\phi_0(\vec{r}) = \frac{P}{h\nu} \frac{2}{\omega^2 \pi} e^{2r^2/\omega^2} \quad (1.7b)$$

$$G(\nu) = \frac{1}{\sqrt{2\pi}\sigma_l} e^{-(\nu-\nu_l)^2/2\sigma_l^2} \quad (1.7c)$$

where  $P$  is the laser power;  $\omega$  is the beam waist;  $\sigma_l$  is the Gaussian width of the laser and  $\nu_l$  is the central laser frequency.

### 1.2.6 Polarization Time Evolution

Polarizations of Rb electrons are more complex, but  $^3He$  nuclei have an intrinsic nuclear spin of  $1/2$ , and it is simpler to explain the math with spin of  $1/2$ . Let's define the polarization as the asymmetry between  $+1/2$  state and  $-1/2$  state:

$$P = \frac{\rho_{+1/2} - \rho_{-1/2}}{\rho_{+1/2} + \rho_{-1/2}} = \rho_{+1/2} - \rho_{-1/2} \quad (1.8)$$

where  $\rho_{\pm 1/2}$  is the population in the  $\pm 1/2$  state.

The time evolution of polarization for both Rb electrons and  $^3He$  follows the equation:

$$\frac{dP}{dt} = \gamma(1 - P) - \Gamma \cdot P \quad (1.9)$$

$\gamma$  is the polarization rate and  $\Gamma$  is the depolarization rate in the above differential equation. The solution has the simple form of:

$$P(t) = Ce^{-(\gamma+\Gamma)t} + \frac{\gamma}{\gamma + \Gamma} \quad (1.10)$$

Note the depolarization rate also contributes to the rate at which  $P$  approaches saturation as it lowers the saturated polarization hence shortens the time to reach it.

The saturated polarization is defined as the value of  $P$  in the limit  $t \rightarrow \infty$ :

$$P_{\infty} = \frac{\gamma}{\gamma + \Gamma} \quad (1.11)$$

The initial polarization is defined as the value of  $P$  at  $t = 0$ :

$$P_0 = C + \frac{\gamma}{\gamma + \Gamma} = C + P_{\infty} \quad (1.12)$$

Thus,  $P(t)$  can be expressed as:

$$P(t) = (P_0 - P_\infty)e^{-(\gamma+\Gamma)t} + P_\infty \quad (1.13)$$

In the case of polarizing Rb with a pump laser,  $\gamma$  is the pumping rate  $R$  and  $\Gamma$  is the Rb spin relaxation rate  $\Gamma_{Rb}$ . There is typically a small angle  $\theta$  between the pump laser and the holding field even though great effort has been made to minimize the angle. Thus  $P(t)$  can be rewritten as:

$$P(t) = P_0 e^{-(R+\Gamma_{Rb})t} + P_{laser} \cos\theta \frac{R}{R + \Gamma_{Rb}} (1 - e^{-(R+\Gamma_{Rb})t}) \quad (1.14)$$

$\theta$  is called the skew angle,  $P_{laser}$  is the circular polarization of the pump laser which is above 99.5%. Rb close to the front side of the cell can reach above 97% (depends on the laser power and other factors) on the order of 100's of microseconds. As the laser propagates through the cell, power is attenuated by Rb vapor. Therefore Rb polarization at the back side of the cell is lower than that at the front side. One way to overcome the problem is to shine pump laser from both sides of the cell which would lead to higher overall Rb polarization and  $^3\text{He}$  polarization.

Spins are thermally polarized with the presence of a magnetic field even without external pumping source. The probability for a spin to be in state  $s$  is:

$$Prob. = \frac{e^{-E_s/k_B T}}{\sum_{st} e^{-E_{si}/k_B T}} \quad (1.15)$$

where  $E_s$  is the energy of the state,  $k_B$  is the Boltzmann constant and  $T$  is the temperature. Using the thermal distribution, under typical operating conditions,  $^3\text{He}$  polarization is  $10^{-9}$  and Rb polarization is  $10^{-5}$ . Both are negligible without active



pumping.

### 1.2.7 Rb Spin Destruction Rate

There are two main mechanisms of Rb depolarization: the binary collisions with Rb,  $^3\text{He}$  and  $N_2$ , and the formation and breakup of van der Waals molecules, the second mechanism is negligible for  $^3\text{He}$  cells. The Rb spin destruction rate can then be expressed as

$$\Gamma_{Rb} = k_{Rb-Rb}[Rb] + k_{Rb-^3He}[^3He] + k_{Rb-N_2}[N_2] \quad (1.16)$$

where  $k_{Rb-X}$  is the spin destruction rate constant and  $[X]$  is the density of X. Dolph has summarized these constants based on measurements from various groups:

$$k_{Rb-^3He}(T) = 55.9(9) \left( \frac{T}{473.15K} \right)^{3.31(12)} Hz/amg \quad (1.17a)$$

$$k_{Rb-N_2}(T) = 290(30) \left( \frac{T}{473.15K} \right)^{2.0(25)} Hz/amg \quad (1.17b)$$

$$k_{Rb-Rb} = 4.813(48) \times 10^{-13} Hz \cdot cm^3 \quad (1.17c)$$

For a pure Rb cell at 170°C with the following densities in the pumping chamber:

$$[^3He] \approx 8.0amg \quad (1.18a)$$

$$[N_2] \approx 0.08amg \quad (1.18b)$$

$$[Rb] \approx 6.0 \times 10^{14} cm^{-3} \quad (1.18c)$$

The approximate spin destruction rates due to various gases are:

$$\Gamma_{Rb-^3He} \approx 360 Hz \quad (1.19a)$$

$$\Gamma_{Rb-N_2} \approx 20 Hz \quad (1.19b)$$

$$\Gamma_{Rb-Rb} \approx 289 Hz \quad (1.19c)$$

The total spin destruction rate is 669 Hz. With more than 20 W narrowband laser, the optical pumping rate is often 100s kHz, which is much greater than the total Rb spin destruction rate. Therefore, it is very easy to achieve a close to unity alkali polarization.

## 1.3 Spin Exchange

Following equation 1.14, the time evolution of  $^3He$  polarization can be expressed as:

$$P_{^3He}(t) = P_0 e^{-(\gamma_{se} + \Gamma)t} + P_{Rb} \frac{\gamma_{se}}{\gamma_{se} + \Gamma} (1 - e^{-(\gamma_{se} + \Gamma)t}) \quad (1.20)$$

The saturation polarization is

$$P_{\infty} = P_{Rb} \frac{\gamma_{se}}{\gamma_{se} + \Gamma} \quad (1.21)$$

where  $\gamma_{se}$  is the spin exchange rate between  $^3He$  and Rb, and  $\Gamma$  is the spin relaxation rate.

### 1.3.1 Spin-Dependent Interactions

The key process in spin-exchange optical pumping is collisional transfer of polarization between optically pumped alkali-metal atoms and the nuclei of the noble gas atoms.

As in Fig. 1.6, the transfer of angular momentum occurs either while the atoms are bound in van der Waals molecules or in simple binary collisions. For  $^3\text{He}$ , binary collisions dominate, and the contribution from van der Waals molecules is negligible. The time scale for binary collisions is on the order of  $10^{-12}$  sec, the collision can induce both  $\Delta F = \pm 1$  and  $\Delta F = 0$  transitions between hyperfine sublevels. For heavier noble gases like  $^{129}\text{Xe}$  at pressure of a few tens of Torr, the contributions of van der Waals molecules can greatly exceed that of binary collisions. At several atmos which is the typical operating pressure for SEOP, the time scale of van der Waals molecules is greatly limited by collision so that the binary collisions dominate.

Spin-dependent interactions produce the spin transfer and relaxation. For SEOP, spin-rotation interaction between  $\vec{S}$  and the rotational angular momentum  $\vec{N}$  of the atom pair formed by Rb and noble gas atom, and the isotropic hyperfine interaction between  $\vec{S}$  and the noble-gas nuclear spin  $\vec{I}_b$  dominate the spin-exchange process:

$$V_1(\vec{R}) = \gamma(R)\vec{N} \cdot \vec{S} + A(R)\vec{I}_b \cdot \vec{S} \quad (1.22)$$

The spin-rotation interaction is caused by the magnetic fields from relative motion of the charges of the colliding atoms, and the isotropic hyperfine interaction comes from the magnetic field inside the nucleus of the noble-gas atom. The spin-rotation interaction produces relaxation of the alkali-metal electron-spins, while the isotropic hyperfine interaction transfers angular momentum back and forth between the alkali-metal electron spins and the noble-gas nuclear spins.

An alkali-metal atom and a noble-gas atom interact via both a large spin-independent interaction  $V_0(R)$  and a small spin-dependent interaction  $V_1(R)$ . At the high oper-

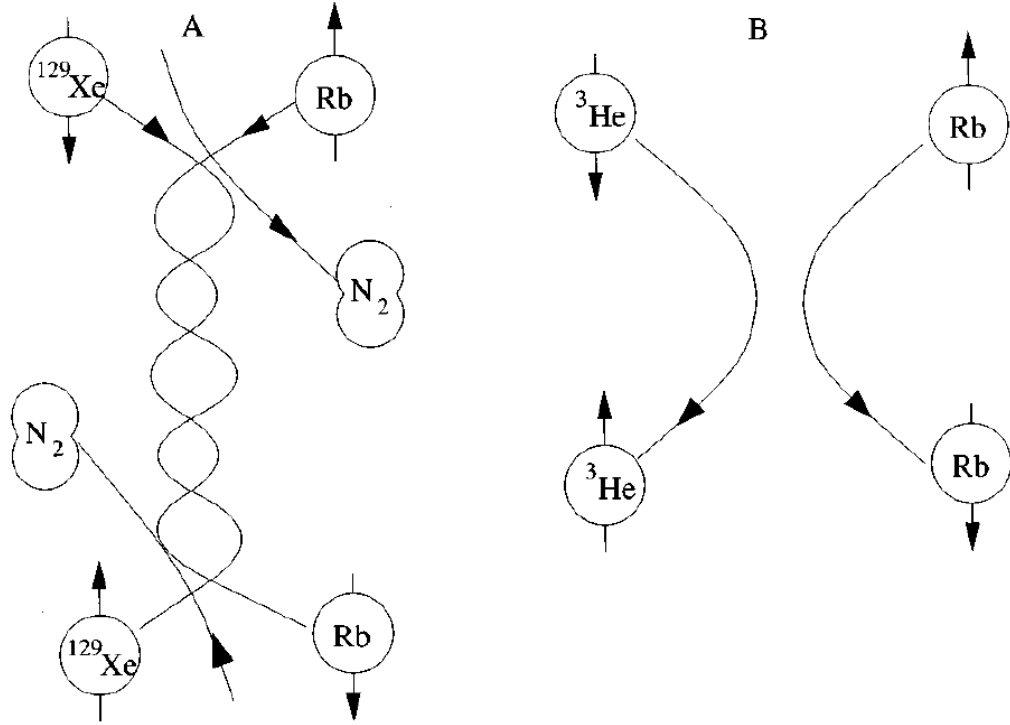


Figure 1.6: A. Formation and breakup of alkali-metal/noble-gas van der Waals molecule. B. Binary collision between an alkali-metal atom and a noble-gas atom. (from Ref. [10])

ating temperatures,  $V_0$  determines classical collision trajectories, while  $V_1$  acts as a small perturbation. We'll focus on  $V_1$  below since it is responsible for spin exchange.

Including a few more terms that were neglected in Eq. 1.7, the spin-dependent interaction  $V_1(R)$  can be expressed as:

$$\begin{aligned}
V_1(\vec{R}) = & \gamma(R) \vec{N} \cdot \vec{S} + \sum_k A_k(R) \vec{I}_k \cdot \vec{S} \\
& + \sum_k B_k(R) \vec{I}_k \cdot (3\vec{R}\vec{R} - 1) \cdot \vec{S} \\
& + \sum_k C_k(R) \vec{I}_k \cdot (3\vec{R}\vec{R} - 1) \cdot \vec{I}_k
\end{aligned} \tag{1.23}$$

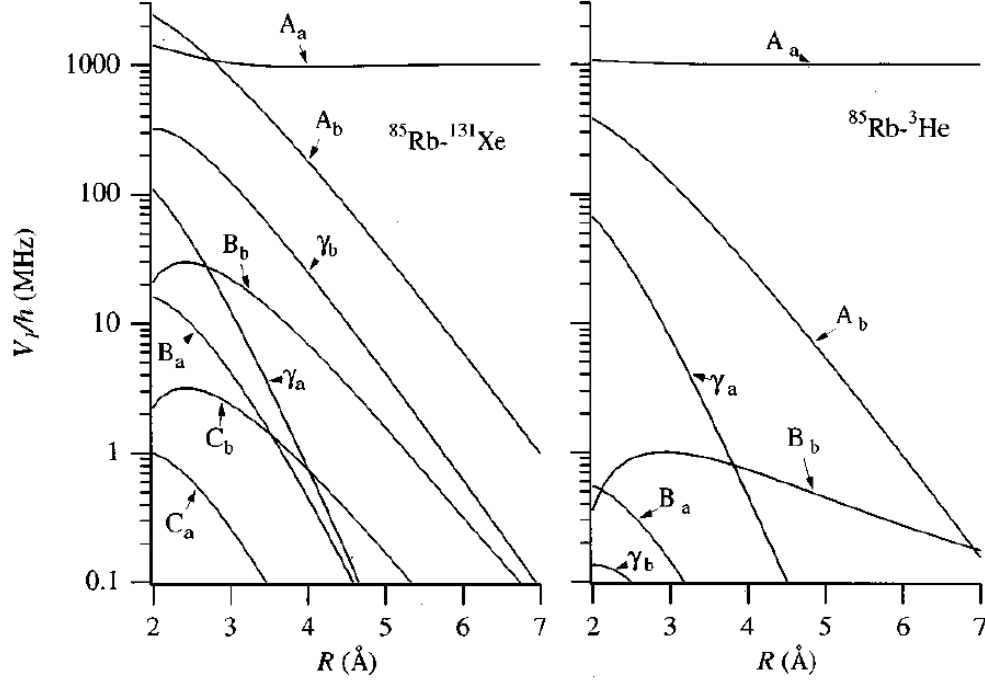


Figure 1.7: Strengths of various spin-dependent interactions as functions of separation (from Ref. [10])

where  $\vec{I}_a$  and  $\vec{I}_b$  are the nuclear spins of the atomic pair, where a stands for alkali metal atom and b stands for noble gas atom.  $\gamma$  is the coefficient of the spin-rotation interaction, while  $A_k$ ,  $B_k$ ,  $C_k$  are the coefficients for isotropic magnetic-

dipole hyperfine interactions, anisotropic magnetic-dipole hyperfine interactions, and electric quadrupole interactions, respectively.  $A_a$  greatly exceed other coefficients as the separations between atoms increase.

The isotropic hyperfine interactions come from the Fermi-contact magnetic fields of the two nuclei.  $A_b$  is the term responsible for spin exchange:

$$A_b(R) = \frac{8\pi g_s \mu_B \mu_b}{3I_b} |\eta \phi_0(R)|^2 \quad (1.24)$$

where  $\eta$  is the enhancement factor which equals to the ratio of the perturbed wave function at the noble gas nucleus to that without the noble gas atom. The isotropic hyperfine interaction also introduces a frequency shift of the magnetic resonance lines for alkali-metal and noble gas atoms. The frequency shift is characterized by another enhancement factor  $\kappa$  which is the ratio of the actual shift of the alkali metal electron lines due to the presence of polarized noble gas nuclei to what would be produced by the bulk magnetization of polarized noble gas. The shift is used in the technique Electron Paramagnetic Resonance (EPR) to calculate the polarization of noble gas nuclei.

The isotropic magnetic-dipole coupling polarizes the noble gas nuclei parallel to the electron spin polarization, while the anisotropic magnetic-dipole coupling polarizes in the opposite direction. Fortunately, the anisotropic interaction is negligible compared to isotropic interaction.

### 1.3.2 Spin Exchange Rate

The spin exchange rate due to binary collisions is:

$$\gamma_{se} = \langle \sigma_{se} v \rangle [Rb] = k_{se} [Rb] \quad (1.25)$$

where  $k_{se} = \langle \sigma_{se} v \rangle$  is the velocity-averaged spin exchange rate constant.  $k_{se}$  for spin exchange between  $^3He$  and Rb is:

$$k_{se}^{^3He-Rb} = (6.7 \pm 0.7) \times 10^{-20} cm^3/s \quad (1.26)$$

Under 170°C which is a typical temperature that we run tests with,

$$[Rb] = 2.60 \times 10^{14} cm^{-3} \quad (1.27)$$

Thus for a single chamber cell,

$$\frac{1}{\gamma_{se}} \approx 15.9 hrs \quad (1.28)$$

## 1.4 $^3He$ Spinup and Relaxation

Similar to the optical pumping process of Rb,  $^3He$  polarization can be described by

$$P_{^3He}(t) = P_0^{^3He} e^{-(\gamma_{se} + \Gamma)t} + P_\infty^{^3He} (1 - e^{-(\gamma_{se} + \Gamma)t}) \quad (1.29)$$

where the saturation polarization is

$$P_\infty^{^3He} = P_\infty^{Rb} \frac{\gamma_{se}}{\gamma_{se} + \Gamma} \quad (1.30)$$

And  $\Gamma$  is the total relaxation rate of  $^3He$  nucleus spin polarization,

$$\Gamma = \Gamma_{dipolar} + \Gamma_{inhomogeneity} + \Gamma_{wall} \quad (1.31)$$

When a target cell are used in electron scattering experiments where an electron beam goes through part of the cell, an additional relaxation rate due to the beam  $\Gamma_{beam}$  should also be included.

The coupling of nuclear spin to orbital angular momentum creates an intrinsic  $^3\text{He}$  relaxation rate that depends on density. At room temperature ( $23^\circ\text{C}$ ), the dipolar relaxation rate is

$$\frac{1}{\Gamma_{dipolar}} = \frac{[^3\text{He}]}{744} \text{hr}^{-1} \quad (1.32)$$

where  $[^3\text{He}]$  is the  $^3\text{He}$  density in amagats. Assuming the cell density is 8 amg, the relaxation rate is  $1/93 \text{ hr}^{-1}$ . In addition, there is an additional intrinsic relaxation due to the spin-rotation interaction. This mechanism dominates the relaxation for  $^{129}\text{Xe}$  but is small for  $^3\text{He}$ .

The relaxation rate due to field inhomogeneities is

$$\Gamma_{inhomogeneity} = D \frac{|\nabla B_x|^2 + |\nabla B_y|^2}{B_0^2} \quad (1.33)$$

where  $D$  is the  $^3\text{He}$  diffusion constant,  $\nabla B_x$  and  $\nabla B_y$  are the transverse magnetic field inhomogeneities,  $B_0$  is the holding field along z-axis. Under operating conditions, assuming the pressure is around 12 atm and field is 12.6 G,  $D \approx 0.16 \text{ cm}^2/\text{s}$  and the field inhomogeneities are 10mG/cm, the relaxation rate is  $1/1400 \text{ hr}^{-1}$ .

Wall relaxation is typically the dominant relaxation mechanism for cells in our lab. This mechanism depends on the property of the inner surface of glass. Most



of the target cells are constructed with reblown General Electric Type 180 (GE-180) glass. This aluminosilicate glass is highly impermeable to  $^3\text{He}$ . The wall relaxation is believed to be associated to several different mechanisms, such as paramagnetic impurities in the glass and microfissures in the surface that could trap  $^3\text{He}$  atoms. It has been found reblowing the glass can help lower the wall relaxation rate because it reduces the number of microfissures. The wall relaxation is not well understood, but it is believed to scale with the surface-to-volume ratio:

$$\Gamma_{wall} = \rho S/V \quad (1.34)$$

where  $\rho$  is called relaxivity.

## 1.5 X Factor

In 2006, Babcock *et al.* reported evidence of a previously unrecognized spin relaxation mechanism, and named it X factor. This mechanism appears to be temperature dependent and roughly proportional to alkali density. The X factor limits the maximally achievable  $^3\text{He}$  polarization even with infinite laser power. The saturation polarization is

$$P_{\infty}^{^3\text{He}} = P_{\infty}^{Rb} \frac{\gamma_{se}}{\gamma_{se}(1 + X) + \Gamma} \quad (1.35)$$

In the presence of infinite laser power where  $\gamma_{se} \gg \Gamma$ , the saturation polarization becomes

$$P_{\infty}^{^3\text{He}} = P_{\infty}^{Rb} \frac{1}{1 + X} \quad (1.36)$$

# Chapter 2

## $^3\text{He}$ Polarimetry

### 2.1 Overview

Traditional pure glass target cells are studied mainly using Adiabatic Fast Passage (AFP) Nuclear Magnetic Resonance (NMR) and Electron Paramagnetic Resonance (EPR). AFP is a technique that allows us to monitor a signal that is directly proportional to the  $^3\text{He}$  polarization, which serves as a means to gain knowledge of properties of cell including the time it takes to polarize it and the relaxation rates of its polarization. The EPR technique utilizes the fact that polarized  $^3\text{He}$  produces frequency shift of the magnetic resonance lines of alkali metal to measure the  $^3\text{He}$  polarization. When AFP and EPR are combined, we can calculate the calibration constant between an AFP signal and the corresponding  $^3\text{He}$  polarization.

A significant focus of my studies is on exploring cells that incorporate metal. Unfortunately, AFP is not suitable for studying these cells as it requires exposing the entirety of the cell to a Radio Frequency (RF) magnetic field in an attempt to flip all

spins in the cell. The RF field would induce an Eddy current induced in the metal body that significantly affects the resulting signal. For these cells, Pulsed Nuclear Magnetic Resonance (PNMR) has proven to be very useful. PNMR only applies a pulsed RF field to a small selected part of the cell which makes it relatively easy to prevent metal from distorting the signal. However, the spins tipped by applying the pulse lose their transverse component (which depends on the "tip angle"), we typically allow some time for this portion of gas to diffuse out of the region being monitored before we can take the next measurement on a fresh sample of the gas. The highest rate at which PNMR measurements can be taken is limited by this requirement.

This chapter introduces the three techniques mentioned above and how they're used for our studies.

## 2.2 Adiabatic Fast Passage

### 2.2.1 Nuclear Magnetic Resonance

The energy of a magnetic moment in an external field is

$$E = -\vec{\mu} \cdot \vec{B}_0 = -\mu_z B_0 \quad (2.1)$$

where  $\vec{\mu}$  is the magnetic moment, for a spin-1/2 nuclei, the energy is

$$E = -\gamma B_0 \hbar / 2 \quad (2.2)$$

$\gamma$  is the gyromagnetic ratio,  $\gamma/2\pi \approx 3.2434 \text{ kHz/Gauss}$ . When an oscillating magnetic field with the frequency  $\omega = \gamma B_0$  is present, transitions between the  $+1/2$  and

-1/2 states are induced. This frequency is called Larmor frequency. When a nucleus is placed in an external magnetic field that is not aligned with its magnetic moment, it will precess at the Larmor frequency.

## 2.2.2 The Rotating Coordinate System

### 2.2.2.1 Classical Formulation

For a nucleus in an external field  $\vec{B}$  with  $\gamma\hbar\vec{I}$  as its nuclear angular momentum, the equation of motion in a stationary coordinate system is [7]

$$\hbar\frac{d\vec{I}}{dt} = \gamma\hbar\vec{I} \times \vec{B} \quad (2.3)$$

Let  $\frac{\partial}{\partial t}$  represent the derivative with respect to a coordinate system that rotates with angular velocity  $\vec{\omega}$ ,

$$\frac{d\vec{I}}{dt} = \frac{\partial\vec{I}}{\partial t} + \vec{\omega} \times \vec{I} \quad (2.4)$$

Substitute Eq. 2.4 into Eq. 2.3,  $\vec{I}$  in the rotating frame satisfies the equation of motion

$$\hbar\frac{\partial\vec{I}}{\partial t} = \gamma\hbar\vec{I} \times (\vec{B} + \vec{\omega}/\gamma) = \gamma\hbar\vec{I} \times \vec{B}_{eff} \quad (2.5)$$

where  $\vec{B}_{eff}$  is the effective field in the rotating frame

$$\vec{B}_{eff} = \vec{B} + \vec{\omega}/\gamma \quad (2.6)$$

Thus, the effective field experienced by an observer in the rotating frame is simply the external field  $\vec{B}$  plus an additional field  $\vec{\omega}/\gamma$ .

If we apply this result to rotating magnetic fields, we will get the core idea of performing an Adiabatic Fast Passage (AFP) measurement. Assuming a constant field  $\vec{B}$  and another field  $\vec{B}_1$  perpendicular to  $\vec{B}$  that is rotating with angular velocity  $-\omega$ . In the rotating frame that rotates with  $\vec{B}_1$ , both aforementioned fields are just constant and the effective field in the rotating frame is

$$B_{eff}\vec{z} = (B - \omega/\gamma)\vec{z} + B_1\vec{x}' \quad (2.7)$$

where  $\vec{x}'$  is the direction that  $\vec{B}_1$  is in. When on resonance ( $B = \omega/\gamma$ ), the effective field is perpendicular to the constant field  $\vec{B}$ .

#### 2.2.2.2 Quantum Mechanical Formulation

The above conclusion can be easily reached with quantum mechanics. The Shrödinger equation for a magnetic moment in an external field is

$$i\hbar\dot{\psi} = \mathcal{H}\psi = -\gamma\hbar\vec{I} \cdot \vec{B}\psi \quad (2.8)$$

Let  $\psi$  and  $\vec{B}$  be the wave function and magnetic field in a stationary frame and  $\psi_r$  and  $\vec{B}_r$  be the same quantities in a rotating frame with angular velocity  $\vec{\omega}$ . Using the rotation operator in quantum mechanics,

$$\psi = e^{-i\vec{\omega} \cdot \vec{I}t} \psi_r \quad (2.9a)$$

$$\vec{I} \cdot \vec{B}_r = e^{i\vec{\omega} \cdot \vec{I}t} \vec{I} \cdot \vec{B} e^{-i\vec{\omega} \cdot \vec{I}t} \quad (2.9b)$$

Substituting 2.9 into Eq.2.8, the Shrödinger equation in the rotating frame is obtained

$$i\hbar\dot{\psi}_r = -\gamma\hbar\vec{I} \cdot (\vec{B}_r + \vec{\omega}/\gamma)\psi_r = -\gamma\hbar\vec{I} \cdot \vec{B}_{eff}\psi_r \quad (2.10)$$

The same effective field in the rotating frame is reached as that from the classical derivation.

### 2.2.3 Adiabatic Fast Passage

Adiabatic Fast Passage (AFP) NMR is used to measure the  $^e\text{He}$  polarization. In an AFP measurement, with the assistance of a oscillating radiofrequency (RF) field, the spins follow the effective field in a rotating frame (as discussed in more detail below) and are flipped 180 degrees to the opposite direction and then flipped back, producing two peaks in signal when they're perpendicular to the holding field and the pick up coils.



as discussed above. The other rotating component that rotates in the opposite direction does not affect the spins. In an AFP measurement, the holding field starts from a value lower than  $\omega/\gamma$  ( $\omega/\gamma - B \gg B_1$ ), so that the effective field is almost aligned with the holding field and the spins. The holding field is then swept at a constant rate through resonance to a value greater than  $\omega/\gamma$ . The sweeping rate is of great importance. The sweep needs to be slow enough so that the nuclear spins can follow the effective field

$$\frac{\dot{B}}{B_1} \ll \omega \quad (2.12)$$

Sweep that satisfies this condition is considered as adiabatic.

Sweep rate cannot be too slow either, because the relaxation rate of the spins are faster near the resonance especially with a small effective field  $B_1$ . The relaxation rate of  $^3\text{He}$  in the rotating frame at resonance is

$$\frac{1}{T_{1r}} = D \frac{|\nabla B_z|^2}{B_1^2} \quad (2.13)$$

where  $D$  is the  $^3\text{He}$  self-diffusion constant. In order to keep the AFP loss low, it's important for the time scale that the spins stay close to resonance to be much shorter than  $1/T_{1r}$ :

$$D \frac{|\nabla B_z|^2}{B_1^2} \ll \frac{\dot{B}}{B_1} \quad (2.14)$$

Typically, the field is swept from 12.6 Gauss to 20.4 Gauss in 6s, thus



$$\dot{B} = 1.3G/s \quad (2.15a)$$

$$B_1 \approx 100mG \quad (2.15b)$$

$$f = 56.6kHz \quad (2.15c)$$

$$D \approx 0.16cm^2/s \quad (2.15d)$$

$$|\nabla B_z| \approx 10mG/cm \quad (2.15e)$$

$$(2.15f)$$

With these operating conditions,

$$D \frac{|\nabla B_z|^2}{B_1^2} \approx 1.6mHz \quad (2.16a)$$

$$\frac{\dot{B}}{B_1} \approx 13Hz \quad (2.16b)$$

$$w \approx 356kHz \quad (2.16c)$$

The AFP conditions are clearly well satisfied. Fig.2.2 shows the evolution of effective field in the rotating frame during an AFP measurement.

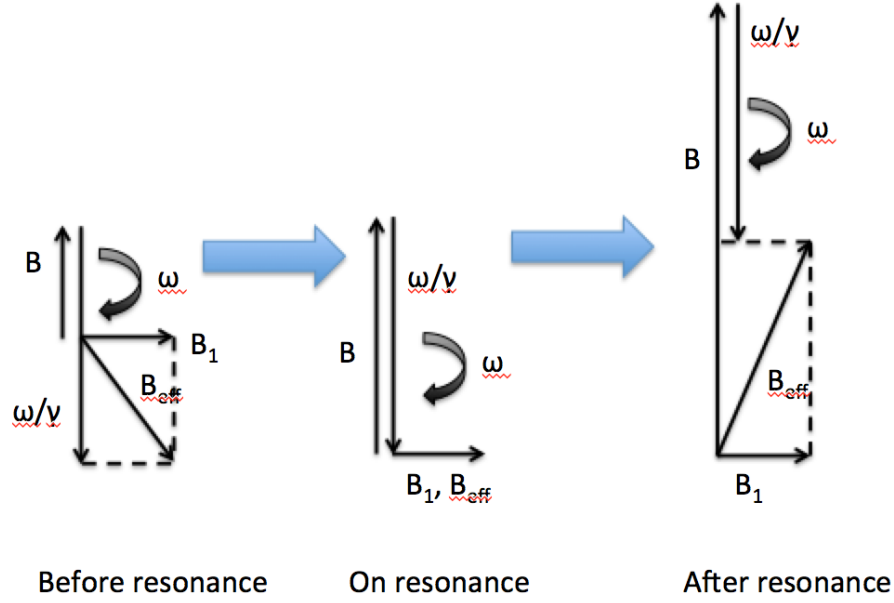


**Figure 2.2: Effective field in the rotating frame during an Adiabatic Fast Passage measurement.** The  $^3\text{He}$  spins follow the direction of the effective field.  $B_1$  is exaggerated to show different components of effective field clearly.

The pick up coils are placed close to the cell and perpendicular to the holding field and RF field. As the  $^3\text{He}$  spins precess along the holding field, the transverse component of the spins will induce an electromotive force (EMF) that is directly proportional to the amplitude of the component in the pick up coils. The signal can be written as:

$$S = A\omega \sin \alpha(t) = A\omega \frac{B_1}{\sqrt{B_1^2 + (B(t) - \omega/\gamma)^2}} \quad (2.17)$$

where  $A$  is a constant that accounts for the cell and coils geometry, the cell magnetization and the electronics factors that affect the size of signal;  $\omega$  is the RF frequency;  $\alpha$  is the angle between the effective field and the holding field in the rotating frame;  $B(t)$  is the holding field as a function of time. The signal reaches peak value when  $B(t) = \omega/\gamma$ . Fig.2.3 shows the result of a typical AFP measurement.

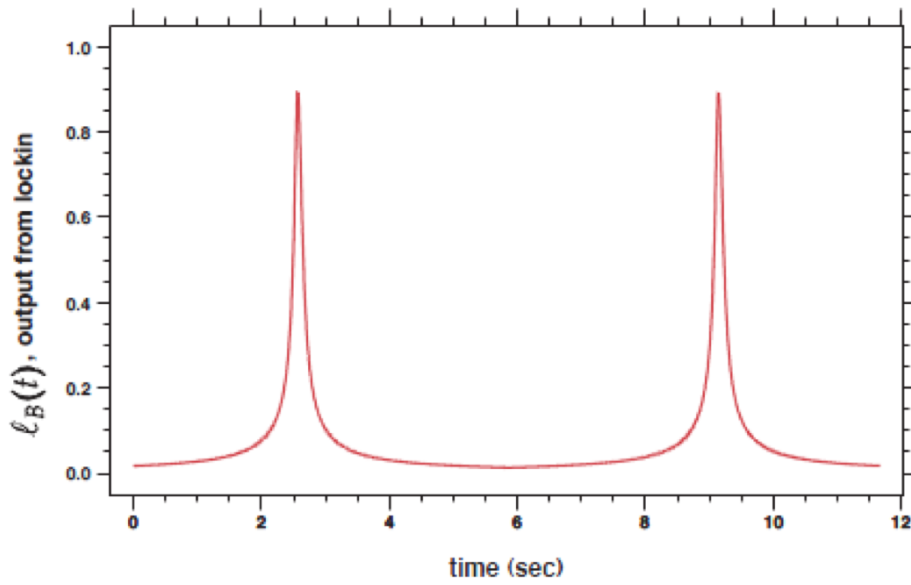


Figure 2.3: A typical AFP signal. y axis is in arbitrary unit.

#### 2.2.4 AFP Loss

The longitudinal spin relaxation rate due to static field inhomogeneities is

$$\frac{1}{T_1} = D \frac{|\nabla B_x|^2 + |\nabla B_y|^2}{B_0^2} \quad (2.18)$$

where  $D$  is the diffusion constant for the polarized spins, and is inversely propor-

tional to the gas pressure.  $B_0$  is the mean magnetic field along z axis.  $B_x$  and  $B_y$  are the x and y components of the magnetic field. However, when performing AFP measurement, the spins are exposed to a small oscillating RF field, the spin relaxation can be greatly accelerated under magnetic resonance conditions [5],

$$\frac{1}{T_{r1}} = \frac{8R^4}{175D} |\nabla\Omega_z|^2 \sum_n \frac{175}{4(\chi_{1n}^2 - 2)(\chi_{1n}^4 + r^2 + r^2 s^2)(1 + s^2)} \quad (2.19)$$

where R is the cell radius, D is the diffusion constant,  $\Omega_z$  is the Larmor frequency of the holding field,  $r = \frac{\omega_r R^2}{D}$ ,  $s = \frac{\Omega_0 - \omega}{\omega_r}$ , the numbers  $\chi_{1n}$  are the zeros of the derivatives of the spherical Bessel functions

$$\frac{d}{dx} j_1(x_{1n}) = 0 \text{ for } n = 1, 2, 3... \quad (2.20)$$

Since  $r^2 \gg \chi_{1n}^4$ , and  $\sum_n \frac{1}{\chi_{1n}^2 - 2} = \frac{1}{2}$  [4],

$$\frac{1}{T_{r1}} = \frac{R^4 |\nabla\Omega_z|^2}{r^2 (1 + s^2)^2 D} = \frac{|\nabla B_z|^2 D}{B^2 (1 + s^2)^2} \quad (2.21)$$

If  $P_0$  is the polarization before AFP, the polarization P after a single AFP flip is given by

$$P = P_0 e^{-\int \Gamma_{r1} dt} = P_0 e^{-\int \frac{1}{T_{r1}} dt} \quad (2.22)$$

Given the field sweep starts from 12.6G, ends at 20.4G, the RF frequency is 56.6kHz, the sweep time is 6s and  $B_1$  is 100mG, we can safely approximate the integral by

$$\int_{-\infty}^{\infty} \frac{1}{T_{r1}} dt = \frac{\pi D |\nabla B_z|^2}{2 B_1 \partial B_1 / \partial t} \quad (2.23)$$

which is the fractional loss due to a single AFP flip.

To better understand AFP loss, we performed a study where we took AFP measurements at various different field gradients to study the relation between AFP loss and inhomogeneities. The gradients were produced by Maxwell-style transverse gradient coils and increased from 0 to a little under 160 mG/cm. At each set gradient, we take one AFP to look at the difference between the two peaks to determine the loss due to a single flip. Fig 2.4 shows AFP losses collected from experiments and theoretical predictions. They agree mostly within the error bar.

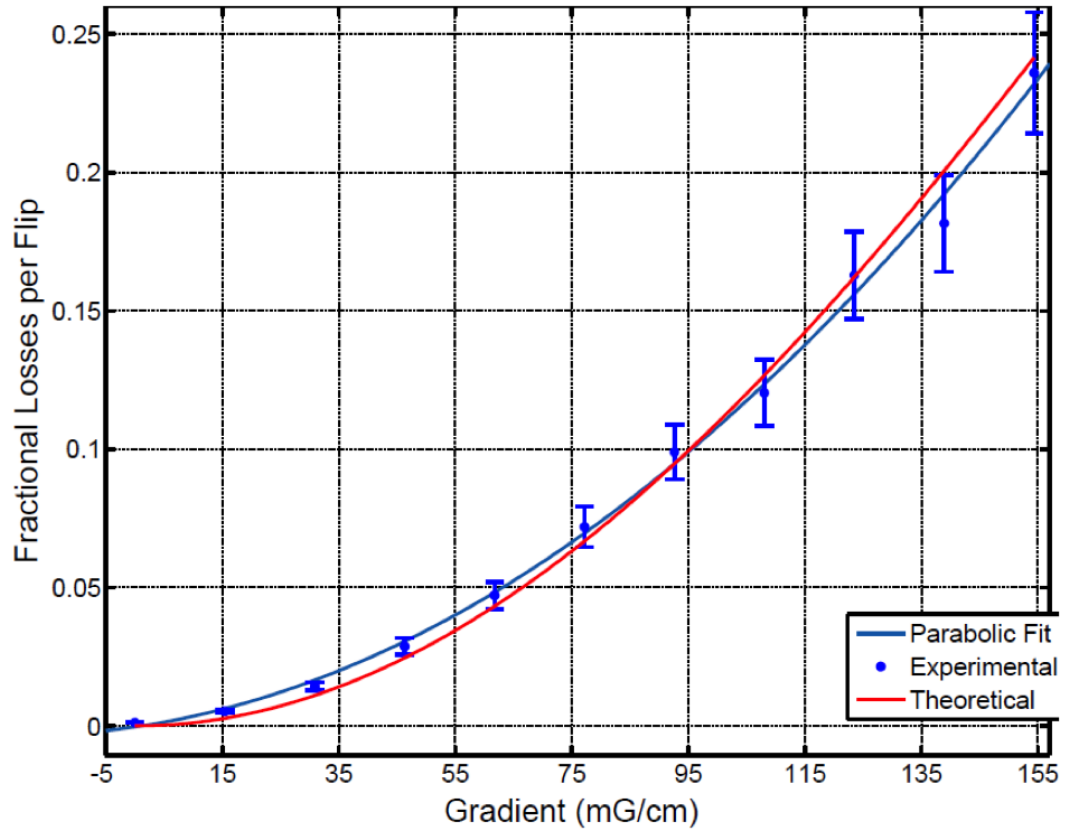


Figure 2.4: Fractional AFP loss (single flip) as a function of field gradient.

## 2.3 Electron Paramagnetic Resonance

### 2.3.1 Overview

Electron Paramagnetic Resonance (EPR) is an important technique for measuring the frequency shift of alkali metal Zeeman resonance due to the effective magnetic field produced by polarized  $^3\text{He}$  gas. The EPR shift is largely caused by the Fermi-contact interaction  $\propto \mathbf{K} \cdot \mathbf{S}$  between the nuclear spin  $\mathbf{K}$  of the noble gas nucleus of magnetic moment  $\mu_K$  and the electron spin  $\mathbf{S}$  of the alkali metal atom [2]. The magnetic field created by the bulk magnetization of the  $^3\text{He}$  gas also contributes directly to a relatively small part of the shift (roughly 1/6 for K). The total measured shift is therefore written as the expected Zeeman interaction with the field produced by the polarized  $^3\text{He}$  multiplied by an enhancement factor  $\kappa_0$ . The enhancement effect comes from overlapping of alkali metal electrons and  $^3\text{He}$  nuclei during binary collisions, thus  $\kappa_0$  is different for each alkali metal species and slightly temperature dependent.

During the process of optical pumping, the Rb atoms are excited to the  $5P_{\frac{1}{2}}$  state by the pump laser. The majority of these atoms are quenched non-radiatively to the ground state by  $\text{N}_2$ . While at  $5P_{\frac{1}{2}}$  state, Rb atoms can also be excited to the  $5P_{\frac{3}{2}}$  state through collisions with other Rb atoms. A small fraction of the excited atoms ( $5P_{\frac{1}{2}}$  and  $5P_{\frac{3}{2}}$ ) decay by emitting either a  $D_1$  photon or  $D_2$  photon. The intensity of fluorescence is proportional to the excited Rb atoms, thus is higher when the Rb polarization is low so more Rb atoms can absorb laser and jump to the excited state. We typically induce Zeeman transitions with a RF coil to lower alkali polarization and detect  $D_2$  photons with a photodiode behind a  $D_2$  filter. The highest amount of  $D_2$  photons is detected when the RF frequency is exactly equal to the Zeeman

transition frequency.

### 2.3.2 The Breit-Rabi Equation

The Zeeman energy levels of ground state ( $L = 0$ ) can be described with the Breit-Rabi equation

$$E_{F=I\pm 1/2, m_F} = -\frac{h\Delta\nu_{hfs}}{2(2I+1)} - \mu_N g_I B m_F \pm \frac{h\Delta\nu_{hfs}}{2} \sqrt{1 + \frac{4m_F x}{2I+1} + x^2} \quad (2.24)$$

where

$$x = (g_I \mu_N - g_s \mu_B) \frac{B}{h\Delta\nu_{hfs}} \quad (2.25)$$

$B$  is the magnetic field,  $\Delta\nu_{hfs}$  is the hyperfine splitting frequency,  $I$  is the nuclear spin,  $g_I$  and  $g_s$  are the  $g$  factors of nuclear and electron spin,  $\mu_N$  and  $\mu_B$  are the nuclear and Bohr magneton, respectively.

The Zeeman transition frequency of  $m_F \rightarrow m_F - 1$  is

$$\begin{aligned} \nu_{m_F \rightarrow m_F - 1} &= \frac{E_{F, m_F} - E_{F, m_F - 1}}{h} \\ &= -\frac{g_I \mu_N B}{h} \pm \frac{\Delta\nu_{hfs}}{2} \left( \sqrt{1 + \frac{4m_F}{2I+1} x + x^2} - \sqrt{1 + \frac{4m_F - 1}{2I+1} x + x^2} \right) \end{aligned} \quad (2.26)$$

The second term is much greater than the first term under our operating conditions, so the sign of the frequency  $\nu_{m_F \rightarrow m_F - 1}$  depends on the second term only. If we focus on the top hyperfine manifold in the energy level graph, the transition frequency is

$$\nu_{m_F \rightarrow m_{F-1}} = -\frac{g_I \mu_N B}{h} + \frac{\Delta \nu_{hfs}}{2} \left( \sqrt{1 + \frac{4m_F}{2I+1}x + x^2} - \sqrt{1 + \frac{4m_F - 1}{2I+1}x + x^2} \right) \quad (2.27)$$

### 2.3.3 Shift of Zeeman Frequency

Under our operating condition, the size of Zeeman splitting is much less than hyperfine splitting, which makes  $x$  a small number. The Taylor expansion of Eq. 2.27 is

$$\begin{aligned} \nu_{m_F \rightarrow m_{F-1}} = & -\frac{g_I \mu_N B}{h} \\ & + \frac{\Delta \nu_{hfs}}{2} \left( \frac{2x}{2I+1} - \frac{2(2m_F - 1)x^2}{(2I+1)^2} + \frac{(-(2I+1)^2 + 4 - 12m_F + 12m_F^2)x^3}{(2I+1)^3} + \dots \right) \end{aligned} \quad (2.28)$$

With the approximation

$$g_s \mu_B \gg g_I \mu_N \quad (2.29a)$$

$$x \approx -\frac{g_s \mu_B B}{h \Delta \nu_{hfs}} \quad (2.29b)$$

To the lowest order approximation, the shift of  $\nu_{m_F \rightarrow m_{F-1}}$  due to a small effective field  $\Delta B$  ( $\Delta B \ll B$ ) from polarized  $^3\text{He}$  is

$$\begin{aligned} \Delta \nu_{m_F \rightarrow m_{F-1}} = & -\frac{g_s \mu_B}{h(2I+1)} \Delta B \left[ 1 + 2(2m - 1) \frac{g_s \mu_B B}{h \Delta \nu_{hfs}(2I+1)} \right. \\ & \left. + 6 \left( -\frac{(2I+1)^2}{4} + 1 - 3m + 3m^2 \right) \left( \frac{g_s \mu_B B}{h \Delta \nu_{hfs}(2I+1)} \right)^2 + \dots \right] \end{aligned} \quad (2.30)$$



Usually the pumping chamber is spherical, the magnetic field produced inside a uniformly magnetized sphere is

$$\Delta \mathbf{B} = \frac{2}{3} \mu_0 \mathbf{M} \quad (2.31)$$

where  $\mu_0$  is the vacuum permeability,  $\mathbf{M}$  is the magnetization of  $^3\text{He}$ ,

$$\mathbf{M} = \mu_K [\text{He}] P \quad (2.32)$$

where  $\mu_K$  is the magnetic moment of  $^3\text{He}$ ,  $[\text{He}]$  is its density, and  $P$  its polarization. As we mentioned before, as a result of the Fermi-contact interaction  $\alpha \mathbf{K} \cdot \mathbf{S}$  between the nuclear spin  $\mathbf{K}$  of the noble gas nucleus and the electron spin  $\mathbf{S}$  of the alkali metal atom, the effective magnetic field from the polarized  $^3\text{He}$  gas is enhanced by a factor of  $\kappa_0$ :

$$\Delta \mathbf{B} = \frac{2}{3} \kappa_0 \mu_0 \mu_K [\text{He}] P \quad (2.33)$$

The enhancement factor  $\kappa_0$  was measured by Romalis *et al.* in 1998 with an error of 1.5% [9]

$$\kappa_0^{Rb-^3He} = 4.52 + 0.00934[T(^{\circ}C)] \quad (2.34)$$

then it was measured by Babcock *et al.* in 2005

$$\kappa_0^{Rb} = 6.39 + 0.00914[T - 200(^{\circ}C)] \quad (2.35a)$$

$$\kappa_0^K = 5.99 + 0.0086[T - 200(^{\circ}C)] \quad (2.35b)$$

$$\kappa_0^{Na} = 4.84 + 0.00914[T - 200(^{\circ}C)] \quad (2.35c)$$

The two results agree within the error. Thus we can calculate  $^3\text{He}$  polarization with the EPR frequency shift.

## 2.3.4 Experimental Methods

### 2.3.4.1 Overview

Under normal operating conditions, hybrid cells with mixture of Rb and K are used. The vapor density of K is an order of magnitude higher than that of Rb, we typically induce the  $m_F = 2 \rightarrow m_F = 1$  (assuming the angular momentum of laser photons is +1)  $^{39}\text{K}$  transition, which lowers the K polarization. Rb-K spin-exchange rate is fast enough that Rb is depolarized almost instantly. This allows more Rb atoms to absorb laser and be excited to the  $5P_{\frac{1}{2}}$  state which in turn produces more  $\text{D}_2$  fluorescence. The  $\text{D}_2$  fluorescence is at maximum intensity when the RF frequency is on resonance for the Zeeman transition.

We first locate the frequency with a frequency-modulated (FM) sweep, and set the RF frequency to the found value. The RF is locked to the frequency (which is slightly changing) that induces maximum  $\text{D}_2$  light with a proportional-integral feedback circuit (P.I. box). This frequency is referred to as EPR frequency and is measured with a counter. To separate the frequency-shifting effect of polarized  $^3\text{He}$  from other sources

that may affect the transition frequency, we flip the  $^3\text{He}$  magnetization by performing a RF frequency sweep. A frequency sweep is chosen rather than a holding field sweep to keep external magnetic field constant, thus reducing factors that affect Zeeman splitting size. By comparing the frequency measured before and after the flip, together with the real temperature inside the pumping chamber, we can calculate the  $^3\text{He}$  polarization. We typically take AFP measurements right before and after the relatively quick EPR measurement, so that a calibration constant that translates AFP signal size to  $^3\text{He}$  polarization can be calculated.

#### 2.3.4.2 Locating Zeeman Transition Frequency

The P.I. box only works well in locking the EPR frequency to the  $m_F = 2 \rightarrow m_F = 1$  K transition when the EPR frequency is close to the transition. Thus the first step in EPR measurements is to locate the Zeeman transition. A frequency-modulated (FM) sweep is performed through a range that covers the Zeeman transition, the range is known from experience or calculation and the P.I. box remains off during the sweep.

The RF frequency is generated by the 18.2MHz voltage-controlled oscillator (VCO). The  $\text{D}_2$  fluorescence is detected with the photodiode and recorded during the sweep. The RF is frequency-modulated by a 200Hz signal, the VCO output at any moment during the sweep can be described as:

$$V_{FM}(t) = V_{C0} \sin(2\pi[f_c + D_f \sin(2\pi f_m t + \phi_m)]t + \phi_c) \quad (2.36)$$

where  $V_{C0}$  is the amplitude of the sweeping RF frequency (carrier),  $f_c$  is the RF frequency that is being swept through a set range,  $D_f$  is the peak frequency deviation,  $f_m$  is the modulating frequency (200Hz in our case),  $\phi_m$  and  $\phi_c$  are the phase of the

modulation frequency and carrier frequency, respectively. Thus the RF frequency is

$$f_{FM}(t) = f_c(t) + D_f \sin(2\pi f_m t + \phi_m) \quad (2.37)$$

here  $f_c(t)$  emphasizes the RF frequency is sweeping over time.

The D<sub>2</sub> light intensity can be described with a Lorentzian function:

$$I(f(t)) = \frac{I_0}{(f_{FM}(t) - f_0)^2 + \Gamma^2} \quad (2.38)$$

where  $f_0$  is the Zeeman transition frequency,  $\Gamma$  is the line width. Keeping the first order term of the Taylor expansion of Eq. 2.38, the D<sub>2</sub> light intensity is

$$I(f(t)) = I(f_c(t)) + \left. \frac{\partial I}{\partial f} \right|_{f=f_c(t)} D_f \sin(2\pi f_m t + \phi_m) \quad (2.39)$$

A lock-in amplifier is used to select only the  $f_m$  term and reduce the noise, the signal picked by the lock-in is

$$s(t) = \left. \frac{\partial I}{\partial f} \right|_{f=f_c(t)} D_f \sin(2\pi f_m t + \phi_m) \quad (2.40)$$

which is the derivative of the Lorentzian function multiplied by a sine function. The FM sweep line crosses zero when the RF frequency is equal to the Zeeman transition frequency (peak of the Lorentzian function), which produces the maximum D<sub>2</sub> light intensity. The region between the lowest and highest points of the derivative line is fitted to a line, and the zero-crossing point of the line is used as the Zeeman transition frequency. Fig. 2.5 shows an FM sweep.

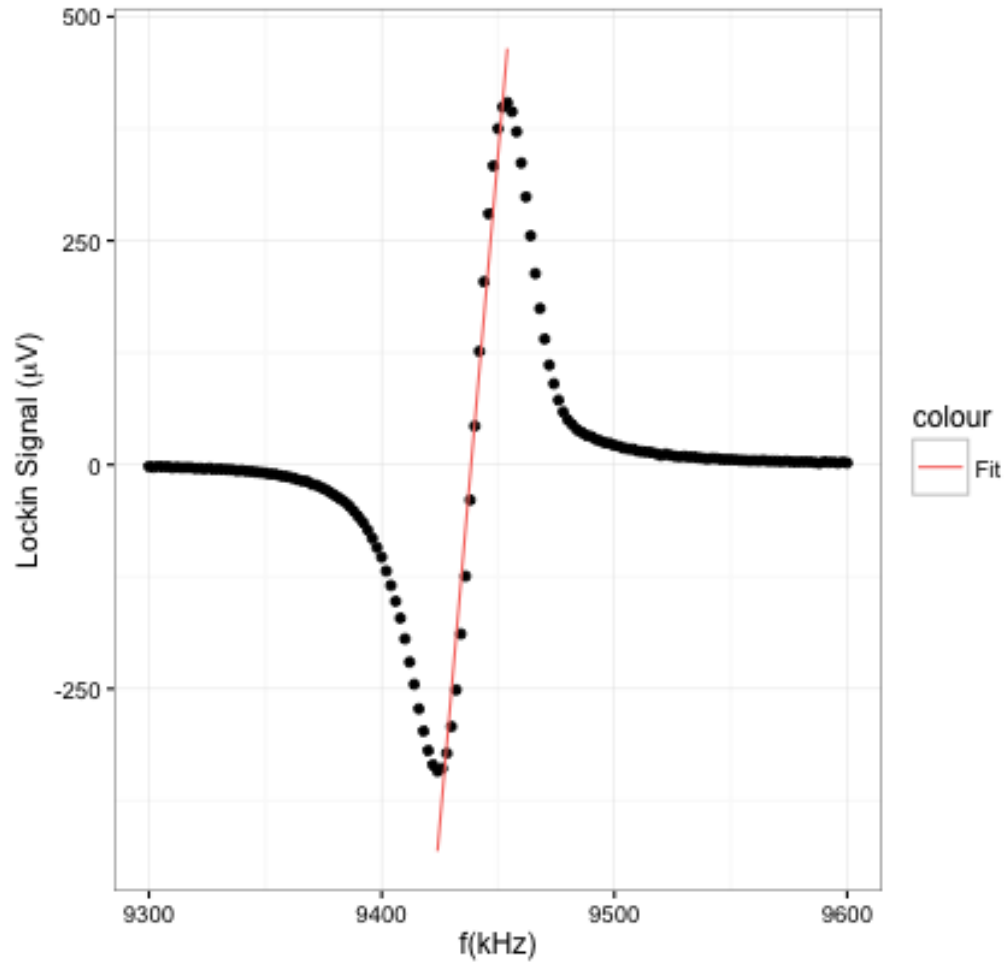
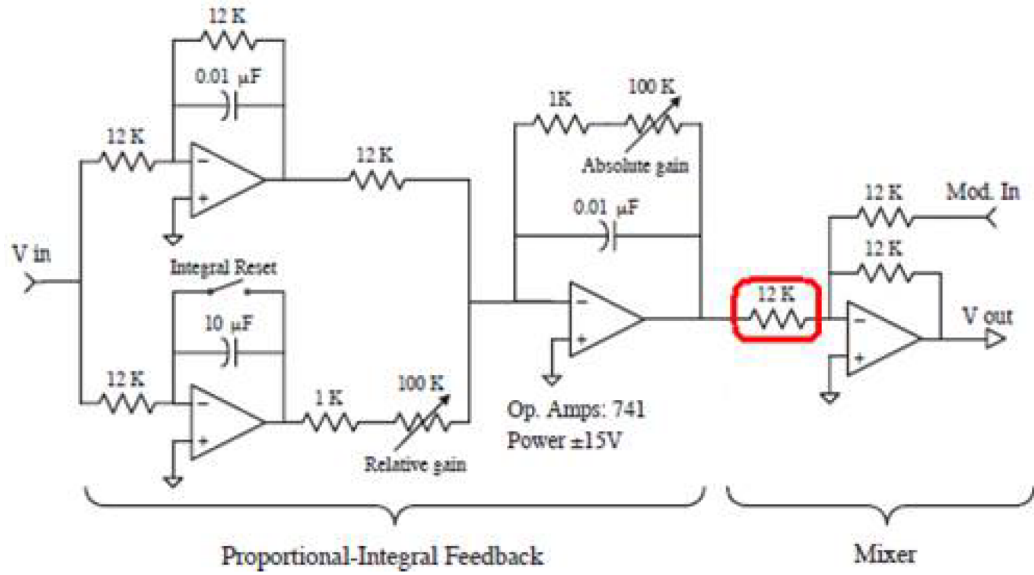


Figure 2.5: A typical FM sweep on a hybrid cell. The central region between the minimum and maximum is fitted to a line. The zero crossing point corresponds to the Zeeman transition frequency.

#### 2.3.4.3 EPR Spin Flip Process

After the transition frequency is located, the VCO frequency is first set to it and then stays locked with a proportional-integral feedback circuit (P.I. box). The circuit is shown in Fig. 2.6.

The output of the lock-in amplifier is sent to the input of the P.I. box, and the



**Figure 2.6:** The same P.I. circuit that was first used by Romalis in our lab. The drawing was then corrected by Peter Dolph.[1]

output of the P.I. box controls the input of the VCO. If the effective magnetic field drifts away from resonance, the P.I. box would receive a non-zero input, and attempt to change the frequency of the VCO output so that its input is zero again. Therefore, the VCO output always matches the transition frequency.

Because the EPR frequency is also affected by sources other than the polarized  $^3\text{He}$  such as the holding field and earth field, we flip the  $^3\text{He}$  spins by sweeping the frequency while keeping the holding field unchanged. The contribution from the flipped spins has a opposite sign while other factors still contribute in the same way which allows us to extract the change of Zeeman transition frequency due to polarized  $^3\text{He}$  and calculate the polarization. We typically let the cell polarization reach saturation before performing EPR measurements. AFP measurements are taken right before and after the EPR measurements for calculating the calibration constant

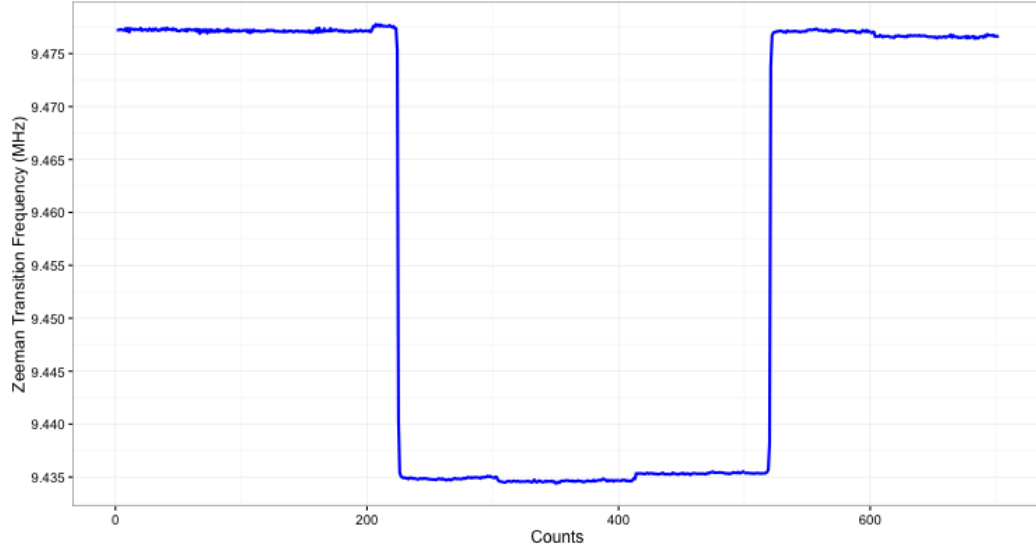


**Figure 2.7: An EPR measurement for a hybrid cell at 235°C.**

The spins are flipped around 200 mark, and flipped back around 500 mark.

(the ratio between polarization and AFP signal size). Fig. 2.7 shows a typical EPR spin flip process.

Under normal operating conditions for a double-chambered cell, the pumping chamber is heated to around 170°C or 235°C depending on if the cell is hybrid, the target chamber and transfer tube remain at room temperature. The temperature difference causes differences in gas densities and affects AFP signal size. Temperature controller of the oven only maintains the surface temperature of the pumping chamber at set temperature, but the gas inside the pumping chamber is always hotter due to absorption of laser energy. The enhancement factor  $\kappa_0$  is also slightly temperature dependent which may be underestimated by  $\sim 4\%$  when using the surface temperature as the gas temperature. Dolph described a method called temperature test to extract gas temperature inside the pumping chamber in detail in his thesis [1]. The idea is to take AFP measurements when the laser is blocked and unblocked multiple times,

assuming the change of gas densities due to absorption of laser is the only reason for the difference in signal size (aside from AFP loss which is compensated through fitting) and the gas temperature when laser is blocked is the same as that measured by RTDs (resistance temperature detectors) on the exterior of the pumping chamber, one can calculate the inside temperature when laser is unblocked.

## 2.4 Pulsed Nuclear Magnetic Resonance

Adiabatic Fast Passage has been the main technique used in our lab for measuring  $^3\text{He}$  polarization through detecting precessing spins with detection coils (we refer to them as pickup coils). In an AFP measurement, all  $^3\text{He}$  spins are flipped by sweeping the holding field while applying a RF field. In more recent studies, we have been exploring the possibility of replacing conventional glass windows with metal end windows in response to the 12 GeV upgrade of JLab. Because of the lack of studies on spin relaxation of polarized  $^3\text{He}$  on metal surfaces, various test cells made with large metal parts as well as glass parts are being studied in our lab. The inclusion of metal parts immediately renders AFP almost useless in the situation because of effects such as Eddy current, thus we have been performing Pulsed Nuclear Magnetic Resonance (PNMR) on metal cells.

### 2.4.1 The Rotating Coordinate System

In a PNMR measurement, a short pulse of RF frequency is applied to a small fraction of  $^3\text{He}$  gas. The RF frequency is tuned to be on resonance at the Larmor frequency of the holding field. As discussed before with AFP, in the rotating coordinate system,



there will be an effective field due to rotation that exactly cancels the holding field which we assume to be in the  $z$  direction. Thus the  $z$  component of the effective field is zero and there is a non-zero constant transverse component which we will call  $B_1$ . The nuclear spins will precess along  $B_1$  and end up at an angle away from  $z$  axis:

$$\alpha = \gamma B_1 \Delta t \quad (2.41)$$

where  $\alpha$  is the angle (tip angle),  $\gamma$  is the gyromagnetic ratio, and  $\Delta t$  is the RF pulse duration.

### 2.4.2 Free Induction Decay

At the end of the RF pulse, the tipped spins will have a transverse component equal to the magnetization multiplied by  $\sin \alpha$ . The spins continue to precess along the holding field and the transverse component will induce a signal in the pickup coils.

In addition to precession, the spins are affected by two types of relaxation processes. The first type is called the spin-lattice relaxation, it describes the rate at which the longitudinal component of magnetization approaches the thermodynamic equilibrium value. It is characterized by the spin-lattice relaxation time constant  $T_1$ . The rate of change of the longitudinal component is

$$\dot{M}_z = -(M_z - M_0)/T_1 \quad (2.42)$$

where  $M_0$  is the thermodynamic equilibrium magnetization. Solving the differential equation gives

$$M_z(t) = M_0 - [M_0 - M_z(0)] e^{-t/T_1} \quad (2.43)$$

The name spin-lattice relaxation refers to the process in which the spins transfer energy to surrounding, thereby restoring their equilibrium state.

The second relaxation process is the transverse relaxation, which is also referred to as the  $T_2$  relaxation and spin-spin relaxation. The transverse component of magnetization decays because variations in the local magnetic field cause different moments to precess at different rates. This is the  $T_2$  process. Normally, the dominating relaxation effect however, is another dephasing process due to inhomogeneities in the holding field over the volume of the cell.

The measured relaxation rate of the tipped spins is the result of all these effects combined:

$$\frac{1}{T_2^*} = \frac{1}{T_2} + \gamma \Delta B_0 \quad (2.44)$$

where  $\Delta B_0$  is the variation in the holding field.  $\gamma \Delta B_0$ , the dominant term, is a spread in Larmor frequencies  $\Delta \omega_0$ , which causes spin-spin dephasing in a characteristic time of  $1/\Delta \omega_0$ .

The time evolution of the nuclear magnetization  $\mathbf{M}$  is described by the Bloch equations [3]:

$$\frac{\partial M_x(t)}{\partial t} = \gamma (\mathbf{M}(t) \times \mathbf{B}(t))_x - \frac{M_x(t)}{T_2^*} \quad (2.45a)$$

$$\frac{\partial M_y(t)}{\partial t} = \gamma (\mathbf{M}(t) \times \mathbf{B}(t))_y - \frac{M_y(t)}{T_2^*} \quad (2.45b)$$

$$\frac{\partial M_z(t)}{\partial t} = \gamma (\mathbf{M}(t) \times \mathbf{B}(t))_z - \frac{M_z(t)}{T_1} \quad (2.45c)$$

where  $\gamma$  is the gyromagnetic ratio and the cross products are the precession terms, the last terms in each equation represent the decaying and dephasing of each component. The precessing spin magnetization generates a signal in the pickup coils that decays with time. This is called free induction decay, the induced signal is of the shape:

$$V(t) = A\omega_0 \sin \alpha \sin (\omega_0 t + \phi) e^{-t/T_2^*} \quad (2.46)$$

where  $A$  is just a constant,  $\omega_0$  is the Larmor frequency for the holding field,  $\alpha$  is the tip angle,  $T_2^*$  is the measured decay time constant. For our metal test cells, depending on the location of the pickup coils and the field setup,  $T_2^*$  varies between several milliseconds to more than 300 milliseconds.

### 2.4.3 Experimental Methods

Our PNMR setup is shown in Fig. 2.8. The Labview program on the computer controls the timing of a gate signal that is fired from the first function generator. The gate signal is fed to the back of the second function generator and triggers it to produce a short pulse. The second function generator sends out RF pulse with pre-set amplitude, duration and frequency only when the gate signal is of voltage higher than

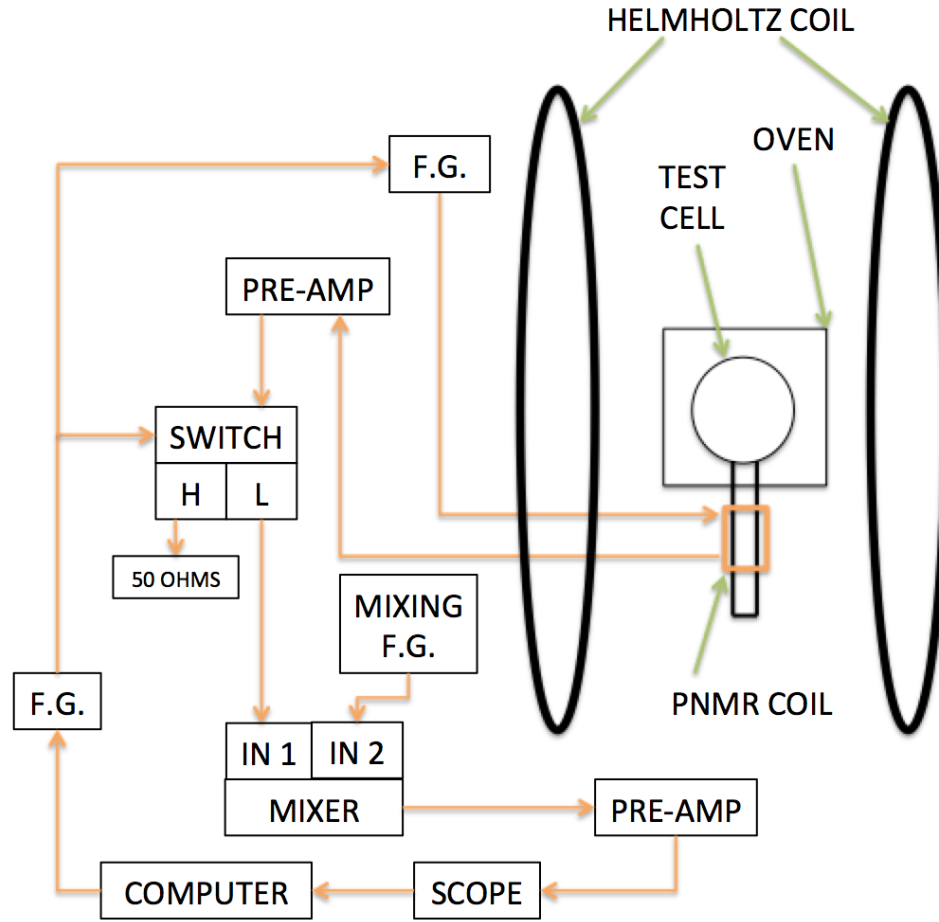


**Figure 2.8: PNMR setup.**

the threshold. The frequency of the RF pulse is carefully tuned to be at the Larmor frequency of the holding field.

The pulse is sent from the function generator to a coil wrapped directly on a small portion of the cell. The spins contained in the coil are exposed to the pulse and tipped by an angle which depends on the amplitude and the duration of the pulse. In the rotating frame, the effective field  $B_1$  causes the spins to precess around it (as discussed before), the precession frequency is  $\gamma B_1$  so the angle the spins rotate by

(tip angle) is

$$\alpha = \gamma B_1 \Delta t \quad (2.47)$$

where  $\gamma$  is the gyromagnetic ratio, the effective field  $B_1$  is directly proportional to the amplitude of the RF pulse,  $\Delta t$  is the duration of the pulse. Ideally, a  $90^\circ$  tip angle would result in the maximum signal, but it has not been the case for us most of the time because of field inhomogeneities. The coils are normally wrapped on the transfer tube of the cell which is off the center of the holding field and exposed to greater inhomogeneities. The details of how we measure the test cells will be discussed in later chapters. Relatively large inhomogeneities cause the spins to precess at different rates, and the dephasing becomes more significant with longer pulse duration and larger tip angle, which leads to non-optimal signal. A typical tip angle for us would be between  $30^\circ$  and  $45^\circ$ .

After the spins are tipped away from z axis, they precess around the holding field and induce a signal in the detection coil. The signal is amplified by a low noise pre-amplifier first and then goes through an isolation switch. The switch only lets signal pass when the controlling gate voltage is low, thus stops the RF pulse from coming back through the detection circuit. The signal is at the Larmor frequency, and is mixed with another frequency after the switch. The mixing frequency is only slightly different from the Larmor frequency, the output of the mixer has both the sum of the two frequencies and the difference. A second pre-amplifier is used to select and amplify the lower of the two frequencies while filtering out high frequency noises. The final output is displayed on a oscilloscope and collected by the Labview program on

the computer. Fig. 2.9 shows a PNMR measurement with around 150 ms decay time constant.

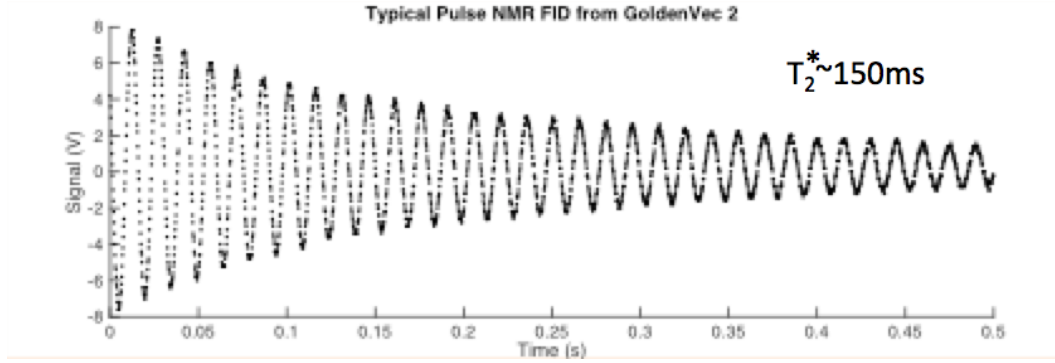


**Figure 2.9: A PNMR signal taken with gold coated test cell.**

The tip angle can be measured with a short sequence of FID signals. Theoretically the tip angle can be calculated with Eq. 2.47. But because of inhomogeneities and other factors, the calculation serves as only an estimate, it is often more accurate and convenient to measure the tip angle directly. We take several PNMR measurements in quick succession with the same RF pulse settings. After every pulse, the transverse component of the spins quickly decay and dephase, leaving only the longitudinal component which is equal to  $\cos \alpha$  times the original magnetization. The intervals between measurements are short enough so that  $T_1$  can be safely ignored. The series of measurements also need to be performed on the same portion of the gas (i.e. the same group of spins tipped by the first pulse), thus it is important to know that the self-diffusion of  $^3\text{He}$  is significantly slower than the sampling rate. The self-diffusion coefficient of  $^3\text{He}$  at 300K is [8]

$$D = \frac{1440(80)torr}{P} cm^2/s \quad (2.48)$$

which is roughly  $1.89 \text{ cm}^2/\text{s}$  at 760 torr (the test cells normally contain around 1 atm of  $^3\text{He}$ ). The diffusion length is described by

$$l = 2\sqrt{Dt} \quad (2.49)$$

Thus in one second, the gas will move around 2.75 cm through self-diffusion. For this reason, we only take 2 or 3 PNMR measurements to calculate the tip angle. As additional measurements would have given enough time for the tipped spins from the first PNMR and the surrounding spins to mix.

Since only the longitudinal component of the tipped spins are preserved, the amplitude of the  $i_{th}$  PNMR is

$$V_i = V_0 \cos^{i-1} \alpha \quad (2.50)$$

where  $V_0$  is the induced signal in the first PNMR. We can then use this equation to calculate the tip angle  $\alpha$ .

# Chapter 3

## Development of Hybrid Targets

### 3.1 Overview

In the first part of this chapter, I present the development of high-performance polarized  $^3\text{He}$  targets for use in electron scattering experiments that utilize the technique of alkali-hybrid spin-exchange optical pumping. Data of 24 separate target cells are presented, each of these cells was constructed while preparing of one of four experiments at Jefferson Laboratory. The results document dramatic improvement in the performance of polarized  $^3\text{He}$  targets. I focus on the data analysis work in this chapter since most of the data had already been taken by the time I joined the group. Other details are described by Jaideep Singh [?]. With the wide range of data, we successfully determined the so-called X-factors that quantify a temperature-dependent and as-yet poorly understood spin-relaxation mechanism that limits the maximum achievable  $^3\text{He}$  polarization to well under 100%. The data collected also served as a measurement of the K- $^3\text{He}$  spin-exchange rate coefficient  $k_{se}^K = (7.46 \pm 0.62) \times 10^{-20}$



cm<sup>3</sup>/s over the temperature range 503 K to 563 K.

In the second part of the chapter, I report the results we have so far on developing the next generation target cell. As mentioned in previous chapters, target cells are composed of two distinct chambers: a pumping chamber (PC) where gas is polarized, and a target chamber through which the electron beam passes. The two chambers are traditionally connected by a single transfer tube. The polarization in the target chamber is replenished by gas from pumping chamber through diffusion. This is not a problem as long as the time scales associated with diffusion are short compared with the time scales associated with the depolarization process. The time scale of diffusion through transfer tube is roughly 0.5-1 hour. Due to the increasing electron beam current, the polarization gradient between the two chambers increased from 1-2% to up about 8% in more recent experiments. Future experiments are likely to use beam currents 4 times or more of what caused 8% polarization gradient. A new design was developed Peter Dolph which circulates the gas with convection instead of diffusion. Dolph demonstrated the design with a prototype cell, later I tested the first and second convection style cells with high <sup>3</sup>He polarization while having convection on. The success with our new design enables future experiment to run with higher electron beam current without causing too much polarization gradient.

## 3.2 Development of Targets without Convection

Spin-exchange optical pumping (SEOP) is a two step process in which an alkali-metal vapor is polarized with optical pumping which subsequently polarizes noble-gas nuclei via spin-exchange collisions. A pure Rb vapor was used to polarize <sup>3</sup>He prior to the

development of hybrid cells. However, it was found that K is far more efficient than Rb at transferring its polarization to  $^3\text{He}$  nuclei. Hybrid mixtures of Rb and K were used more and more frequently to improve the efficiency of the polarization process. In alkali-hybrid spin-exchange optical pumping (AHSEOP), the Rb vapor is polarized by circularly polarized laser, but the polarization of Rb valence electrons is then rapidly shared with the K. The rate at which Rb and K exchange polarization is so fast that their polarizations can be thought of as being equal. If the alkali-hybrid mixture contains significantly more K than Rb with appropriate ratio, the spin-exchange efficiency is greatly improved so that the rate at which  $^3\text{He}$  is polarized is increased significantly for a given amount of laser power.

The second factor that proved to have improved target cells performance greatly was the use of spectrally-narrowed diode lasers. We were able to achieve higher alkali polarization with the aid of these lasers, which in turn reduced the required laser power. The origins of the improved cell performance are twofold. Firstly, these narrowband lasers have spectral profiles closely match the Rb  $D_1$  absorption line shapes, which results in higher optical pumping rates and hence higher alkali polarizations. Secondly, it allows us to use higher alkali densities (which increases spin-exchange rates) without sacrificing alkali polarization.

The data collected over the years include  $^3\text{H}$  polarization achieved under different operating conditions, the time constants of polarization process, the geometric properties of the target cells, and cell fill information such as pressure and ratio of K to Rb in hybrid mixtures, the time constants of spin relaxation process. In roughly half the cells, the alkali polarization and alkali density were also measured with Faraday Rotation techniques. The results contain several thousand hours worth of data and

provide valuable information for future cell development.

Two figures of merit (FOMs) are plotted in Fig. 3.1, both of which are relevant in evaluating the performance of a polarized  $^3\text{He}$  target. The one on the left axis is the effective luminosity  $\mathcal{L}^{eff} = \mathcal{L}P_{He}^2$ , where  $\mathcal{L}$  is the luminosity for a fixed-target experiment (the product of beam current, target density, and interaction length) and  $P_{He}$  is the  $^3\text{He}$  polarization. The luminosity  $\mathcal{L}$  represents the number of scattering opportunities per unit time per unit area, while  $P_{He}^2$  accounts for the reduction in statistical error of some polarization-dependant asymmetry. The FOM on the right axis is used to quantify the potential effective luminosity of a target. The definition is  $\mathcal{L}^N = \mathcal{N}\Gamma_s P_{He}^2$ , where  $\mathcal{N}$  is the total number of  $^3\text{He}$  atoms in the target,  $\Gamma_s$  is the rate at which polarization builds up. The target cell Antoinette is the first one with such high value of  $\mathcal{L}^N$ , which indicates tis cell could tolerate higher luminosities than previously achieved. The high potential further demonstrates the importance of the development of the new convection style target cell. With even higher luminosities in electron scattering experiments, significantly faster gas transfer becomes quite necessary to reduce the polarization gradient between the pumping chamber of target chamber.

### 3.2.1 Experimental Methods

#### 3.2.1.1 The $^3\text{He}$ Targets

Chapter 2 has already described single-chambered cell polarization dynamics to some extent as it is a simpler model for introducing spin-exchange optical pumping. The  $^3\text{He}$  target cells JLab uses for electron scattering experiments usually include two

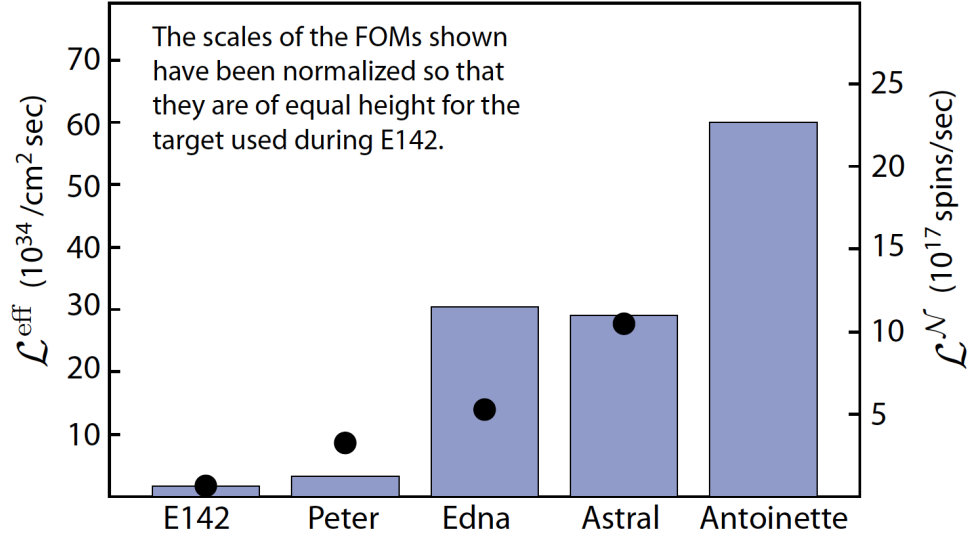


**Figure 3.1:** Shown are two figures of merit (FOM) for targets built for the indicated experiments. The circles (left axis) indicate the number of spins being polarized per second weighted by the square of polarization. The bars (right axis) represent the luminosity weighted by the square of polarization. While the first FOM is an indication of the potential of the polarization technique, the second FOM indicates performance achieved during an experiment. The actual cells used to formulate the FOMs are not necessarily the same.

chambers, a pumping chamber (PC), which is placed in an oven and pumped by circularly polarized laser, and a target chamber (TC) that the electron beam passes through. Fig.3.2 shows a typical cell.

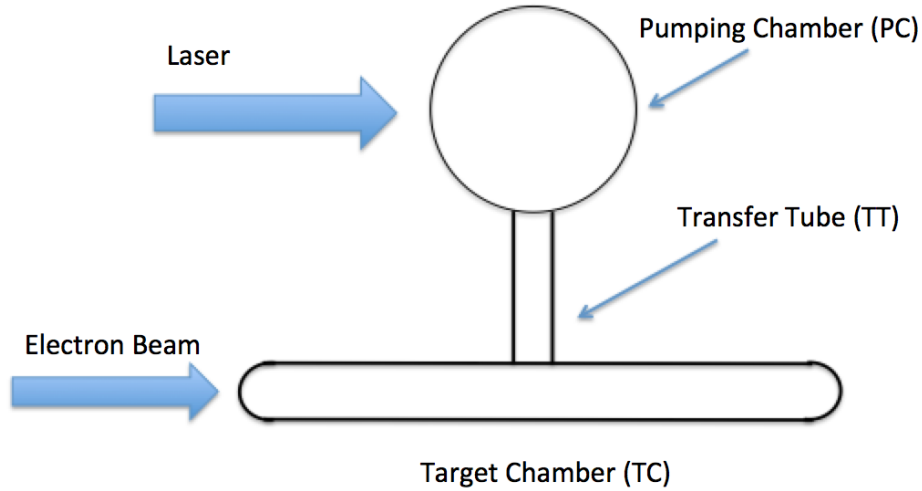


**Figure 3.2: A target cell. The dimensions of different parts of the cell are not to scale.**

After baking the cell to remove moisture and other contaminants, mixtures of Rb and K are chased into the cell. Once the cell has been pumped with a diffusion pump for about a week, we can fill the cell with  $N_2$  and  $^3\text{He}$ .

The  $^3\text{He}$  density is of great importance for characterizing the target cells as it is required in many of the calculations I will discuss later in the chapter. One way to determine the  $^3\text{He}$  density is to through measurements during the cell-filling process. A carefully calibrated volume, together with pressure and temperature measurements gives the volume of different spaces in the gas system (the system that is used to pump the cell and fill it with  $N_2$  and  $^3\text{He}$ ) and the cell. By comparing the amount of  $^3\text{He}$  left in the system, the amount that went into the cell is obtained. The volume of the

cell can be measured by determining its buoyancy force in water. The  $^3\text{He}$  density is determined to within about 1% with the method.

Another method used quite often for determining the  $^3\text{He}$  density through measurements of the pressure broadening of the  $D_1$  and  $D_2$  absorption lines with a scannable single-frequency laser. This measurement also provides the value of  $D$ , which is the ratio of K vapor density to Rb vapor density. Although the value of  $D$  is for the temperature at which the measurement is performed, its value for operating condition can be inferred with alkali-metal vapor pressure curves.  $D$  is also measured with the Faraday Rotation technique in many cases, and the two methods agree with each other quite well. The fill densities and geometric properties of the aforementioned 24 cells are shown in Table 3.1.

### **3.2.1.2 Target Cell Polarization Dynamics**

As previously mentioned, AFP is used to monitor the polarization of  $^3\text{He}$ . An exact value of polarization remains to be calibrated with EPR, but the signal size is directly proportional to the polarization, thus is an indication of how the polarization changes relatively. Two processes that are monitored with AFP are spinups and spindowns.

The process of  $^3\text{He}$  gaining polarization through spin-exchange with Rb that is being constantly pumped by circularly polarized laser is called a spinup. A typical example of a spinup is shown in Fig. ??.

EXP	Cell	Total Volume(cc)	PC Volume(cc)	ill F Density(amg)	TC length(cm)
saGDH	Proteus	235.9	90.8	6.88	34.3
	Peter	208.6	111.3	8.80	39.4
	Penelope	204.3	102.2	8.93	39.7
	Powell	213.3	111.6	8.95	40.5
	Prasch	257.7	114.5	6.94	35.3
GEN	Al	168.4	90.2	8.91	38.4
	Barbara	386.2	306.8	7.60	38.7
	Gloria	378.2	298.8	7.40	38.4
	Anna	386.8	303.7	8.09	38.7
	Dexter	181.4	99.3	9.95	38.7
	Edna	378.3	290.3	7.47	38.7
	Dolly	378.3	293.5	7.42	38.7
	Simone	219.5	118.6	8.17	37.9
	Sosa	388.8	304.7	7.96	38.7
Transversity and $d_2^n$	Boris	246.1	166.1	8.08	38.4
	Samantha	259.0	176.9	7.97	38.4
	Alex	278.3	193.9	7.73	39.1
	Moss	269.8	184.7	7.92	38.7
	Tigger	271.7	186.9	7.81	38.7
	Astral	251.4	164.9	8.18	38.4
	Stephanie	244.3	164.9	8.10	38.5
	Brady	249.9	169.3	7.88	38.4
	Maureen	268.5	177.4	7.63	39.8
	Antoinette	437.8	351.8	6.57	40.3

**Table 3.1:** The table contains the names, total and pumping chamber volumes, fill densities and target chamber lengths of the 24 target cells. The fill densities are the average of the results from gas system measurements and pressure broadening measurements.

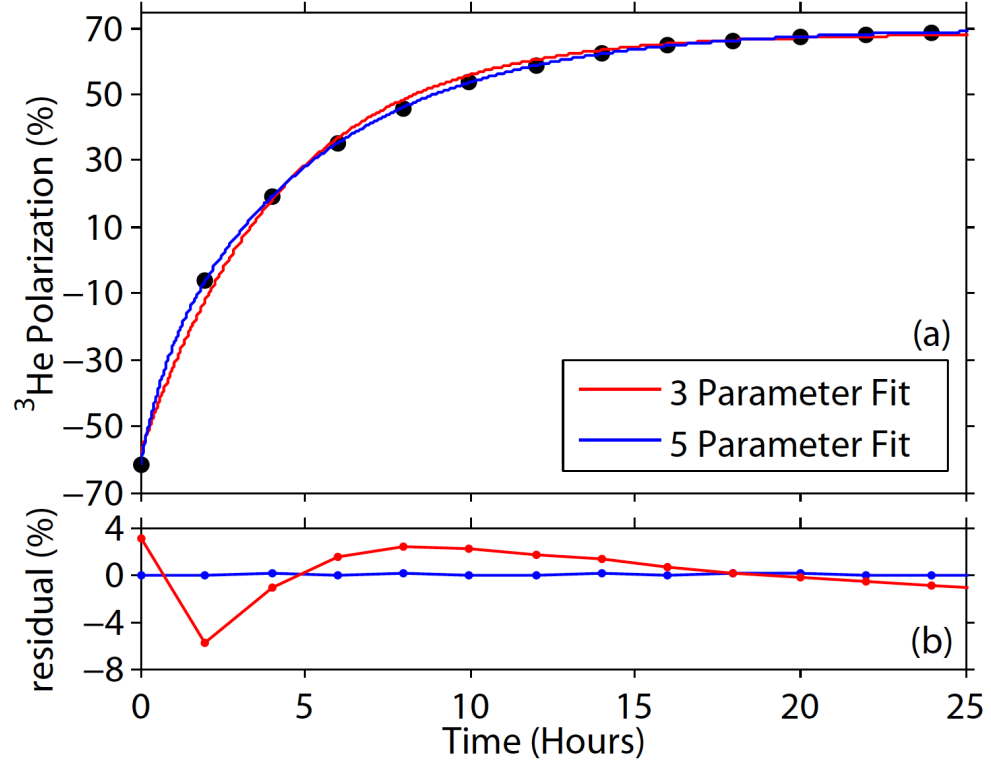


**Figure 3.3:** (a) Shown is a spinup of the target Brady. The spinup data has been fit with a 3-parameter and a 5-parameter formalism. (b) The residuals of the two fits. The error for 3-parameter fit is larger because it does not account for diffusion between two chambers. Adopted from [?].

The equation that describes spinups of single-chambered cell is:

$$P(t) = (P^0 - P^\infty)e^{-\Gamma_{sc}t} + P^\infty \quad (3.1)$$

where  $P^\infty$  is the saturation polarization,  $P^0$  is the initial polarization,  $\Gamma_{sc} = \gamma_{se}(1 + X) + \Gamma$  is the spin up rate of the buildup of polarization. The subscript "sc" here stands for "single chamber" to differ from the spinup rate of double-chambered



cell.  $\gamma_{se}$  is the spin-exchange rate,  $X$  is the  $X$  factor that limits the maximal achievable polarization, which will be discussed in more detail later in the chapter.  $\Gamma$  is the spin relaxation rate. When using this equation to fit spinup, there are only three parameters, hence the name 3-parameter fit. The saturation polarization is given by:

$$P^\infty = \frac{\langle P_A \rangle \gamma_{se}}{\Gamma_{sc}} = \frac{\langle P_A \rangle \gamma_{se}}{\gamma_{se}(1 + X) + \Gamma} \quad (3.2)$$

where  $\langle P_A \rangle$  is the polarization of the alkali vapor averaged over the cell.

The following derivation will only focus on double-chambered cell. The polarization accumulation rate can be described by

$$\frac{dP_{pc}}{dt} = \Gamma_{se}(P_A - P_{pc}) - \Gamma_{pc}P_{pc} - d_{pc}(P_{pc} - P_{tc}) \quad (3.3a)$$

$$\frac{dP_{tc}}{dt} = -\Gamma_{tc}P_{tc} + d_{tc}(P_{pc} - P_{tc}) \quad (3.3b)$$

where  $P_{pc}(P_{tc})$  is the  $^3\text{He}$  polarization in PC (TC);  $\gamma_{se}$  is the spin-exchange rate in PC;  $\Gamma_{pc}(\Gamma_{tc})$  is the relaxation rate of  $^3\text{He}$  polarization in PC (TC);  $d_{pc}(d_{tc})$  is the probability for a nucleus to leave PC (TC) and enter TC (PC). The transfer rates  $d_{pc}$  and  $d_{tc}$  are related by:

$$f_{pc}d_{pc} = f_{tc}d_{tc} \quad (3.4)$$

where  $f_{pc}(f_{tc})$  is the fraction of atoms in PC (TC). The solutions to Eq.3.3 are

$$P_{pc}(t) = C_{pc}e^{-\Gamma_f t} + (P_{pc}^0 - P_{pc}^\infty - C_{pc})e^{-\Gamma_s t} + P_{pc}^\infty \quad (3.5a)$$

$$P_{tc}(t) = C_{tc}e^{-\Gamma_f t} + (P_{tc}^0 - P_{tc}^\infty - C_{tc})e^{-\Gamma_s t} + P_{tc}^\infty \quad (3.5b)$$

where  $P_{pc}^0(P_{tc}^0)$  is the initial polarization in the pumping (target) chamber,  $P_{pc}^\infty(P_{tc}^\infty)$  is the saturation polarization in the pumping (target) chamber. The "slow" time constant  $\Gamma_s$  is mostly determined by the volume averaged spin-exchange rate, which is given by

$$\Gamma_s = \langle \gamma_{se} \rangle (1 + X) + \langle \Gamma \rangle - \delta\Gamma \quad (3.6)$$

where  $\langle \gamma_{se} \rangle = f_{pc}\gamma_{se}$  is the cell averaged spin-exchange rate,  $\langle \Gamma \rangle$  is the cell averaged spin relaxation rate, as the rate might be different for pumping chamber and target chamber. The quantity  $\delta\Gamma$  contains corrections due to the finite speed at which polarization moves between the two chambers. The size of  $\delta\Gamma$  is usually no more than 10% of the size of  $\Gamma_s$  in our studies, and never more than 15%.

Detailed discussion is done by Dolph??. Again, the name 5-parameter fit comes from the fact that there are 5 parameters in each of the two equations. It's interesting to note the time evolution of  $^3\text{He}$  polarization for double-chambered cells has a new time constant: the "fast" time constant  $\gamma_f$  that is dominated by the diffusion rates  $d_{PC}$  and  $d_{TC}$  when diffusion is relatively fast. In the fast-transfer limit, double-chambered solution reduces to single-chambered solution.

The other interesting point is the relation between the saturation polarization in PC and TC

$$P_{tc}^{\infty} = \frac{P_{pc}^{\infty}}{1 + \frac{\Gamma_{tc}}{d_{tc}}} \quad (3.7)$$

In the fast-transfer limit where  $d_{tc} \gg \Gamma_{tc}$ ,  $P_{tc}^{\infty} = P_{pc}^{\infty}$ .

### 3.2.1.3 Initial Spinup

As shown in Fig.3.4, the early behavior of spinup with zero polarization for the pumping chamber and the target chamber are quite different. The initial part of the pumping chamber is almost linear but the target chamber shows a curved initial part. By performing a Taylor expansion on Eq. 3.5 we obtain the initial part of the spinup for both chambers:

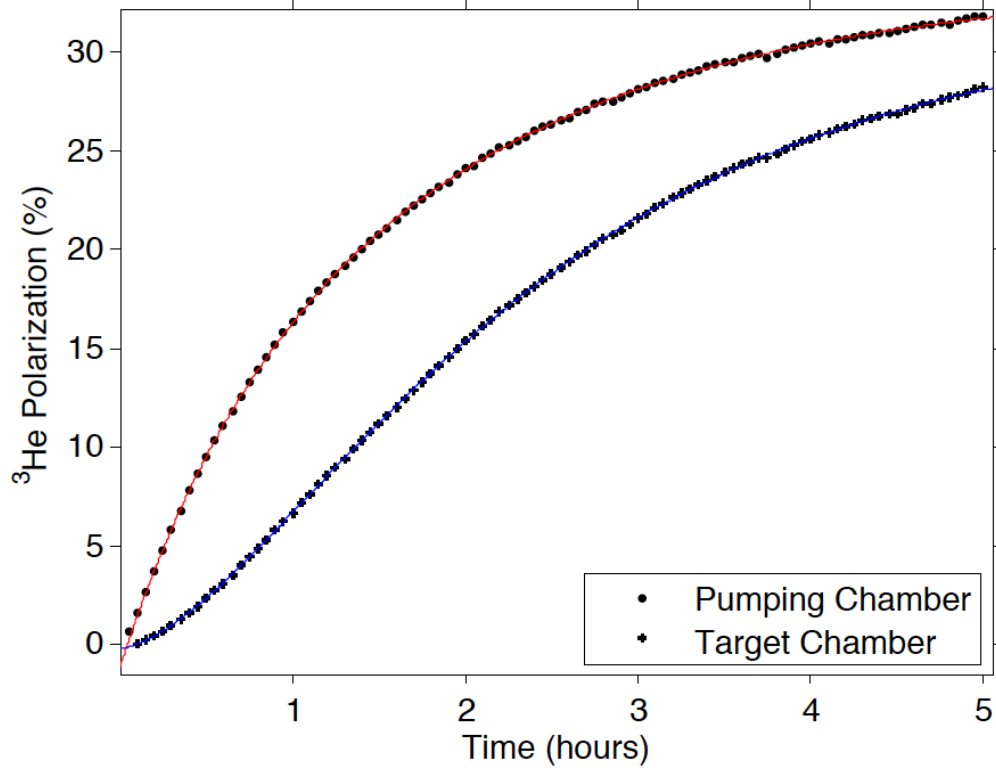


Figure 3.4:  $^3\text{He}$  polarization as a function of time for both the pumping chamber and the target chamber. The top curve is the pumping chamber and the bottom curve is the target chamber. Data was taken at a fast pace so there would be enough points to demonstrate the initial behavior.

$$P_{pc}(t) = \gamma_{se}P_A t - \frac{1}{2}\gamma_{se}P_A(\gamma_{se} + \Gamma_{pc} + d_{pc})t^2 \quad (3.8a)$$

$$P_{tc}(t) = \frac{1}{2}\gamma_{se}P_A d_{tc}t^2 \quad (3.8b)$$

where  $\gamma_{se}$  is the spin-exchange rate in the pumping chamber and  $P_A$  is the alkali polarization. It's clear that the dominant term in  $P_{pc}(t)$  is the linear term while the

shape of  $P_{tc}(t)$  is quadratic.

The slope of the linear shape of initial spinup of the pumping chamber gives access to the product  $P_A\gamma_{se}$  and fitting the initial spinup of the target chamber to a quadratic function provides the product  $\gamma_{se}P_Ad_{TC}$ . The alkali polarization  $P_A$  can be measured with a technique named Faraday Rotation, we then gain knowledge of the spin-exchange rate  $\gamma_{se}$  and the diffusion rate  $d_{tc}$ . The slope of the polarization buildup in the pumping chamber is often written as  $m_{pc} = P_A\gamma_{se}$ .

The spin relaxation rate is also of great importance for characterizing target cells. The relaxation rates in the pumping chamber and the target chamber are different due to geometric and other properties. The cell-average relaxation rate can then be written as

$$\langle\Gamma\rangle = f_{pc}\Gamma_{pc} + f_{tc}\Gamma_{tc} \quad (3.9)$$

where  $f_{pc}$  ( $f_{tc}$ ) is the fraction of atoms in PC (TC);  $\Gamma_{pc}$  ( $\Gamma_{tc}$ ) is the average relaxation rate in PC (TC). When the cell is being pumped by laser, the pumping chamber is heated with hot air to create alkali vapor while the target chamber remains at the room temperature. Difference in temperature further complicates difference in relaxation rates between the two chambers. However, when trying to measure the life time (the inverse of the relaxation rate) of the cell, we typically keep the entire cell at room temperature and perform a "spindown" measurement.

During a spindown, the cell starts with some polarization (normally as high as possible so we can obtain a more complete curve), and relaxes on its own while we take AFP measurements at a certain rate. Typically, the interval between measurements

is anywhere between 30 mins and 2 hrs, depending on the lifetime of the cell. The rule of thumb is to take AFP frequently enough so the spindown curve has sufficient data points while not too often so the polarization relaxes too fast due to AFP losses. The  $^3\text{He}$  polarization relaxation can be described by

$$P(t) = P_0 e^{-t/\tau_{true}} \quad (3.10)$$

The true lifetime  $\tau_{true}$  of the cell without relaxation due to AFP loss can be measured with two methods: the first is to take 5 AFP measurements consecutively with very short interval (normally around 3 minutes), the second is to perform several spindown measurements, each with a different interval.

In the first method, because the lifetime of the cell is much longer than 3 minutes, we can safely attribute all losses to AFP measurements and extract the loss due to a single AFP  $loss_{afp}$ . The data values can then be corrected with the equation

$$S_i^{corrected} = S_i^{raw} / (1 - loss_{afp})^{i-1} \quad (3.11)$$

where  $S_i^{corrected}$  is the corrected signal,  $S_i^{raw}$  is the raw signal,  $i$  represents it is the  $i$ th measurement in the spindown,  $loss_{afp}$  is the loss due to a single measurement. Fitting the corrected values to Eq. 3.10 gives the true lifetime  $\tau_{true}$ .

A simple example for the second method would be to perform one spindown with one-hour interval and another spindown with two-hour interval, the relaxation rates in these two spindowns are

$$\frac{1}{\tau_{1hr}} = \frac{1}{\tau_{true}} + \Gamma_{AFP\_1hr} \quad (3.12a)$$

$$\frac{1}{\tau_{2hr}} = \frac{1}{\tau_{true}} + \Gamma_{AFP\_2hr} \quad (3.12b)$$

$$\Gamma_{AFP\_1hr} = 2 \times \Gamma_{AFP\_2hr} \quad (3.12c)$$

where  $\tau_{1hr}$  and  $\tau_{2hr}$  are the lifetimes measured with taking AFP every 1 hour and every 2 hours,  $\tau_{true}$  is the true lifetime of the cell without interference from measurements,  $\Gamma_{AFP\_1hr}$  ( $\Gamma_{AFP\_2hr}$ ) is the relaxation rate due to taking measurements every 1hr (2hr). We can then solve for  $\tau_{true}$ .

#### 3.2.1.4 The K-<sup>3</sup>He Spin-Exchange Rate Constant

As mentioned in the initial spinup section, the polarization in the pumping chamber at the beginning of accumulation process if started with completely unpolarized state can be described by

$$P_{pc} = \gamma_{se} \langle P_A \rangle (t - t_0) + b(t - t_0)^2 = m_{pc}t + bt^2 + c \quad (3.13)$$

where  $m_{pc}$  is the slope of the linear term. Typically, in the first 20 to 30 minutes, the spinup behaves so linearly that the effect of quadratic term is negligible.

During these initial spinups, an AFP measurement was taken every 3 minutes. The AFP losses were carefully accounted for when calculating  $m_{pc}$ . The <sup>3</sup>He spins were flipped to the opposite direction during every AFP measurement for a short period of time while still receiving polarization in the original direction. Care was taken to account for the time during which spins were "anti-aligned". We refer to the the slope collected from initial spinups as  $m_{pc}^s$ , to differentiate it from the same quantity measured with the Faraday Rotation technique. I will briefly introduce Faraday Rotation, the details were described thoroughly by Dolph. [1].

The Faraday Rotation technique, as the name implies, is the observation of Faraday rotation using a linearly polarized probe laser. Faraday rotation refers to the change in the orientation of the polarization axis when linearly polarized light passes through a polarized alkali vapor. It is sufficient to consider only the alkali-metal atom's D<sub>1</sub> and D<sub>2</sub> lines for our case, the Faraday rotation angle  $\phi_r$  is:

$$\phi_r(\nu) = \left(\frac{r_e c}{6}\right) P_A \cos(\theta) [Rb] l \{F_{Rb}(\nu) + D F_K(\nu)\} \quad (3.14)$$

where  $r_e$  is the classical electron radius,  $c$  is the speed of light in vacuum,  $l$  is the path length through the vapor,  $D$  is the ratio of the K to Rb vapor number densities,  $F_A(\nu)$  is the frequency dependence of alkali species A.

During a Faraday Rotation measurement,  $\phi_r$  was measured at several probe wavelengths and fit to the Eq. 3.14. We were able to obtain the quantities  $P_A[Rb]l$  and  $D$  from the fit. However, in order to extract  $[Rb]$ , it is necessary to measure the path length  $l$  and  $P_A$ . Alkali polarization was measured by measuring the Faraday rotation angle while inducing Zeeman transition. It is worth noting this only gave line-averaged polarization as only information on the path of the probe laser was collected. The volume-averaged alkali polarization can be obtained by applying small corrections from our simulation.

With knowledge of alkali densities, the spin-exchange rate is:

$$\gamma_{se} = k_{se}^{Rb}[Rb] + k_{se}^K[K] \quad (3.15)$$

where  $k_{se}^{Rb}(k_{se}^K)$  is the spin-exchange rate constant between <sup>3</sup>He and Rb (K). The  $m_{pc}$  calculated with this manner is referred as  $m_{pc}^F$ , since this quantity was computed



with Faraday rotation data.

The values of  $m_{pc}^F$  and  $m_{pc}^s$  are expected to be the same if they are measured against the same cell under identical conditions. The spin-exchange rate constants  $k_{se}^{Rb}$  and  $k_{se}^K$  are required to calculate  $m_{pc}^F$ .  $k_{se}^{Rb}$  has been measured and reported in literature multiple times.  $k_{se}^K$  on the other hand, is not as well-known. The value of  $k_{se}^{Rb}$  we used was the combined result from Baranga *et al.* [?] and from Chann *et al.* [?]:

$$k_{se}^{Rb} = (6.79 \pm 0.14) \times 10^{-20} \text{cm}^3/\text{s} \quad (3.16)$$

The ratio of  $m_{pc}^F/m_{pc}^s$  is plotted in Fig. ???. The two measurements with the Rb only cell Sosa are shown with solid circles. To calculate the ratio for the rest of the measurements, a value for  $k_{se}^K$  is needed. Babcock reported this number to be  $(5.5 \pm 0.4) \times 10^{-20} \text{cm}^3/\text{s}$  in his thesis. However, the resulting ratio was significantly lower than unity in all but one of the 6 measurements, as shown with open diamonds in the figure. We fit our data so the ratio  $m_{pc}^F/m_{pc}^s$  is equal to one while treating  $k_{se}^K$  as a free parameter. The results are shown with solid diamonds. Our fitted  $k_{se}^K$  value is

$$k_{se}^K = (7.46 \pm 0.62) \times 10^{-20} \text{cm}^3/\text{s} \quad (3.17)$$

The reason why our result is significantly higher than Babcock's is unclear. One possibility may be temperature dependence as the temperatures under which our measurements were made were higher than that of Babcock's. We decided to use our own result of  $k_{se}^K$  to measure the X factor because it was measured under similar

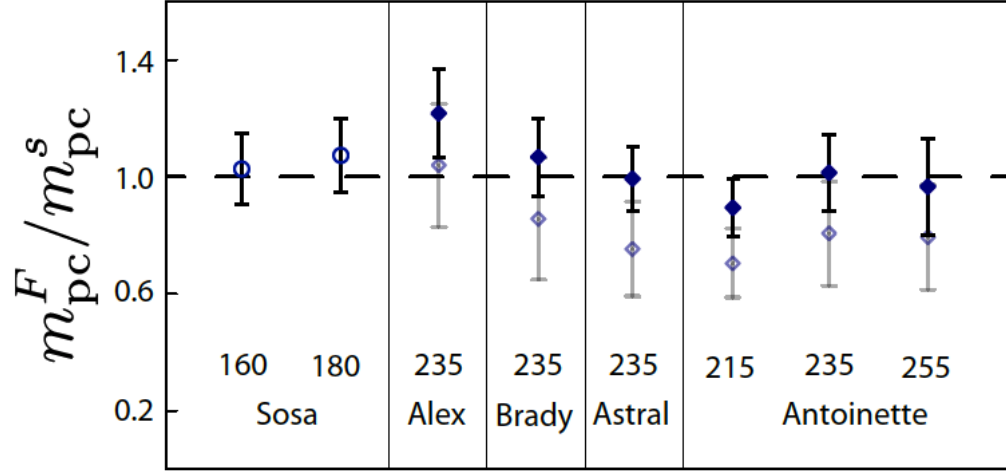


**Figure 3.5:** Plotted is the ratio  $m_{pc}^F/m_{pc}^s$  for eight separate measurements. The numbers above the cell names are the oven set temperatures at which the measurements were made.

operating conditions to our other measurements, and our own result improves internal consistency of our data.

### 3.2.1.5 The X Factor

Prior to the introduction of the X factor, it was believed that  $^3\text{He}$  polarization could approach unity with sufficiently high alkali vapor densities and laser power such that  $P_A$  is nearly 100% and  $\gamma_{se} \gg \langle \Gamma \rangle$ . However, the  $^3\text{He}$  polarization during our studies had shown differently. The fact that it was never close to 100% even with high laser power and alkali densities could be explained by the X factor.

As mentioned earlier, Babcock *et al.* reported a previously unrecognized spin relaxation mechanism in his paper [?]. This mechanism appears to be roughly proportional to the spin-exchange rate  $\gamma_{se}$ , so it cannot be overcome by increasing the

alkali density or laser power. The maximal achievable  $^3\text{He}$  polarization can be expressed as

$$\lim_{\gamma_{se} \rightarrow \infty} = \lim_{\gamma_{se} \rightarrow \infty} \frac{\langle P_A \rangle \langle \gamma_{se} \rangle}{\langle \gamma_{se} \rangle (1 + X) + \langle \Gamma \rangle} = \frac{P_A}{1 + X} \quad (3.18)$$

The combination of alkali-hybrid and narrowband laser has made it much easier to achieve higher spin-exchange rates  $\gamma_{se}$ . Thus X factor is playing an increasingly more significant role in limiting the equilibrium  $^3\text{He}$  polarization, which makes it an important subject of study.

Unlike many other properties of the cell that could be measured directly, X factor is a derived quantity. While characterizing our target cells, we collected enough data to determine X factor in several different ways. We were able to compare these values and combine them into weighted averages. We also looked at possible temperature dependence using X values obtained at different temperatures. The data used is presented in Table 3.2.

We calculated the X factors in 4 different ways, all of which required knowledge of the cell-averaged spin relaxation rate  $\langle \Gamma \rangle$  at operating temperatures. However, the spindown measurements we performed only gave us the spin relaxation rate  $\langle \Gamma \rangle_c$  at room temperature. We made the assumption that the difference between  $\langle \Gamma \rangle$  and  $\langle \Gamma \rangle_c$  is purely due to the change of cell-averaged  $^3\text{He}$ - $^3\text{He}$  dipolar spin relaxation rate, and the relaxation rate due to collisions with the walls is the same for the two chambers and does not change at different temperature. The correction to the relaxation rate is given by

EXP	Cell	Lasers	$I_0$ W/cm <sup>2</sup>	$T_{pc}^{set}$ °C	$P_{He}^\infty$	$\Gamma_s^{-1}$ hrs	$\langle \Gamma \rangle^{-1}$ hrs	$\langle P_A \rangle$	$P_A^l$	$D_{fr}$	$D_{pb}$	$[Rb]_{fr}$ 10 <sup>14</sup> /cm <sup>3</sup>	$\Delta T_{Rb}$ °C	$\Delta T_{He}$ °C	X
saGDH	Proteus	3B	3.8	180	0.46	27	74	-	-	0	0	-	-	-	-
	Priapus	3B	3.8	180	0.44	21	56	-	-	0	0	-	-	-	-
	Penelope	3B	3.8	180	0.39	18	46	-	-	0	0	-	-	-	-
	Powell	3B	3.8	180	0.38	13	25	-	-	0	0	-	-	-	-
	Prasch	3B	3.8	180	0.33	13	33	-	-	0	0	-	-	-	-
GEN	Al	2.5B	3.2	235	0.53(03)	7.86(05)	27.42(1.37)	-	-	-	4.53(25)	-	-	-	-
		5B	6.1	235	0.54(03)	6.73(18)	27.42(1.37)	-	-	-	4.53(25)	-	-	-	-
	Barbara	2.5B	1.6	235	0.37(02)	5.5(08)	42.95(2.15)	-	-	-	4.80(25)	-	-	-	-
		5B	3.1	235	0.57(03)	4.76(63)	42.95(2.15)	-	-	-	4.80(25)	-	-	-	-
	Gloria	3B	1.7	235	0.60(03)	6.13(04)	38.29(1.91)	-	-	-	7.20(40)	-	-	-	-
	Anna	1B	0.6	235	0.33(02)	5.60(34)	11.38(57)	-	-	-	9.64(57)	-	-	-	-
		1.5B	1.0	235	0.39(02)	5.37(08)	11.38(57)	-	-	-	9.64(57)	-	-	-	-
	Dexter	1.5B	1.5	235	0.47(02)	7.58(17)	18.45(92)	-	-	-	-	-	-	-	-
		5B	6.1	235	0.49(02)	6.63(12)	18.45(92)	-	-	-	-	-	-	-	-
	Edna	3B	2.4	235	0.56(03)	5.71(02)	27.42(1.37)	-	-	-	3.63(20)	-	-	-	-
		3B	1.0	235	0.43(02)	6.16(03)	35.24(1.76)	-	-	-	20(1.3)	-	-	-	-
	Dolly	1N1B	1.4	235	0.62(03)	5.79(07)	35.24(1.76)	-	-	-	20(1.3)	-	-	17(10)	-
	Simone	2N1B	3.8	215	0.31(01)	14.08(06)	22.87(1.14)	0.947(020)	0.91(05)	10.66(54)	8.89(45)	0.20(02)	-7(3)	-	-0.04(12)*
		2N1B	3.8	240	0.48(02)	6.89(20)	22.87(1.14)	-	-	-	9.76(49)	-	-	-	-
		2N1B	3.8	255	0.58(02)	6.45(10)	22.98(1.14)	0.929(023)	0.92(05)	12.48(83)	10.3(52)	0.90(09)	-4(5)	-	0.11(06)*
	Sosa	2N1B	1.9	160	0.57(02)	16.69(09)	73.68(3.68)	0.966(020)	1.00(03)	0	0	1.97(13)	4(1)	30(7)	0.24(06) <sup>†</sup>
		2N1B	1.9	170	0.61(03)	11.67(04)	73.68(3.68)	0.964(020)	0.98(03)	0	0	3.00(33)	3(3)	38(14)	0.27(06)*
		2N1B	1.9	180	0.55(02)	8.79(09)	73.68(3.68)	0.954(022)	0.97(03)	0	0	4.30(27)	1(2)	47(7)	0.43(06) <sup>†</sup>
		2N1B	1.9	190	0.40(02)	6.39(22)	73.68(3.68)	0.854(075)	0.82(03)	0	0	5.69(63)	-2(3)	48(20)	0.58(12)*
		2N1B	1.9	200	0.26(01)	5.04(17)	73.68(3.68)	-	-	0	0	-	-	43(18)	-
Transversity	Boris	3B	1.8	235	0.42(02)	6.25(04)	23.74(1.19)	0.871(050)	0.79(07)	1.96(18)	2.45(23)	2.19(34)	-8(7)	-	0.26(10)*
	Samantha	3B	1.8	235	0.50(02)	6.30(13)	36.51(1.83)	-	-	-	4.34(23)	-	-	-	-
		3N	2.6	235	0.68(03)	4.62(03)	22.13(1.11)	0.956(020)	0.99(03)	4.37(10)	4.34(23)	1.80(10)	7(2)	21(10)	0.12(05)*
	Alex	2N1B	2.6	235	0.59(03)	4.81(02)	32.96(1.65)	0.942(042)	0.99(03)	1.37(08)	1.19(07)	4.08(36)	0(4)	42(10)	0.34(06) <sup>†</sup>
	Moss	1N1B	1.8	235	0.62(03)	5.35(04)	33.00(1.65)	-	0.95(09)	-	2.40(13)	-	-	29(8)	-
	Tigger	1N1B	1.8	235	0.51(02)	4.89(05)	12.62(63)	-	0.95(09)	-	-	-	-	23(9)	-
	Astral	2N1B	2.6	235	0.69(03)	6.57(12)	48.90(2.45)	0.954(020)	0.99(03)	7.09(55)	6.21(56)	0.97(09)	3(5)	25(4)	0.17(05) <sup>†</sup>
	Stephanie	3N	2.6	235	0.63(03)	4.55(09)	48.35(2.42)	0.929(114)	0.99(03)	1.39(11)	1.50(10)	5.08(58)	7(5)	54(6)	0.31(08)*
	Brady	1N	0.9	235	0.62(03)	4.82(1.08)	33.50(1.68)	-	0.95(03)	-	2.36(24)	-	-	14(9)	-
		2N	1.8	235	0.68(03)	5.52(70)	33.50(1.68)	-	0.99(03)	-	2.36(24)	-	-	25(8)	-
		3N	2.6	235	0.70(03)	5.30(01)	33.50(1.68)	0.956(021)	0.99(03)	2.60(20)	2.36(24)	2.86(30)	6(5)	39(9)	0.14(05) <sup>†</sup>
	Maureen	3N	2.6	235	0.66(03)	5.42(12)	29.21(1.46)	-	0.97(09)	-	4.42(55)	-	-	32(12)	-
	Antoinette	3N	1.7	215	0.49(02)	6.63(37)	20.93(1.05)	0.958(020)	0.99(03)	2.85(13)	-	0.96(07)	0(3)	16(8)	0.28(08) <sup>†</sup>
		3N	1.7	235	0.61(03)	4.18(10)	20.93(1.05)	0.936(043)	0.99(03)	3.32(27)	-	1.83(20)	0(5)	20(10)	0.24(07) <sup>†</sup>
		3N	1.7	255	0.41(02)	2.66(11)	20.93(1.05)	0.776(099)	0.93(10)	3.57(23)	-	2.88(39)	-5(6)	33(9)	0.55(13) <sup>†</sup>

**Table 3.2:** Cell Performance for three sets of experiments: saGDH (top), GEN (middle), and Transversity &  $d_2^n$  (bottom). Within each experiment grouping, data is grouped by type of laser used (B = Broadband, N = Narrowband).  $I_0$  is the nominal incident laser intensity at the center of the pumping chamber.  $T_{pc}^{set}$  is the oven set temperature.  $P_{pc}^\infty$  is the equilibrium polarization in the pumping chamber and  $\Gamma_s$  is the slow time constant extracted from the five parameter fit to the polarization build up curve.  $\Gamma_c$  is the cell-averaged room temperature spin relaxation rate.  $\langle P_A \rangle / P_A^l$  is the volume averaged to line averaged alkali polarizaition ratio determined from the optical pumping simulation.  $P_A^l$  is the measured line averaged alkali polarization.  $D_{fr}$  &  $D_{pb}$  are the K to Rb density ratios determined from Faraday rotation and pressure broadening measurements.  $[Rb]_{fr}$  is the Rb number density measured from Faraday rotation.  $\Delta T_{He}$  is the temperature of Rb inferred from the number density relative to the oven set temperature.  $\Delta T_{He}$  is the temperature of <sup>3</sup>He inferred from temperature tests relative to the oven set temperature. X is the best combined value for the X-factor. \* indicates X was measured using only spinup, alkali polarization, and Faraday rotation data. <sup>†</sup> indicates X was also measured using the early-time behavior of the spinup.

$$\langle \Gamma \rangle = \langle \Gamma \rangle_c - [n_0 - f_{pc}n_{pc}/f^d(t_{pc}) - f_{tc}n_{tc}/f^d(t_{tc})]/\tau^d \quad (3.19)$$

where  $n_0$  is the  $^3\text{He}$  fill density,  $n_{pc(tc)}$  is the  $^3\text{He}$  density in the pumping (target) chamber,  $f_{pc(tc)}$  is the fraction of  $^3\text{He}$  atoms in the pumping (target) chamber,  $t_{pc} = T_{pc}/(296.15K)$ ,  $t_{tc} = (313.15K)/(296.15K)$ ,  $\tau^d = 744hrs \cdot amg$ ,  $f^d(t)$  is a function that parameterizes the temperature dependence of the dipolar relaxation [?].  $\langle \Gamma \rangle$  for is typically only a few percent less than  $\langle \Gamma \rangle_c$  for us. In addition, whenever the quantity  $(\Gamma_s - \langle \Gamma \rangle)$  is used, a small correction to account for the AFP losses is added.

Our methods of extracting X require using some form of the equation

$$\langle \gamma_{se} \rangle = \frac{\Gamma_s - \langle \Gamma \rangle + \delta\Gamma}{1 + X} \quad (3.20)$$

One method Babcock used and we applied on a small number of cells is called "hot relaxation method". We plot  $\langle \gamma_{se} \rangle$  as a function of  $\Gamma_s - \langle \Gamma \rangle + \delta\Gamma$ , the slope of a linear fit to the data is expected to be  $1/(1+X)$ . Three such fits are shown in Fig. ??, all of which were constrained to go through the origin. Two of the three X values were significantly different than zero. The X factor of Simone is too close to zero when taken the error into account for us to make a strong statement.

The small correction  $\delta\Gamma$  came into play because of the double-chambered design. It can be approximated by

$$\delta\Gamma \approx f_{pc}f_{tc}(d_{pc} + d_{tc})u^2 + \text{higher order terms} \quad (3.21)$$

where  $d_{pc(tc)}$  is the probability per unit time that a  $^3\text{He}$  atom will exit the pumping (target) chamber. The quantity u is

$$u = \frac{\gamma_{se}(1 + X) + \Gamma_{pc} - \Gamma_{tc}}{d_{pc} + d_{tc}} \quad (3.22)$$

where  $\Gamma_{pc(tc)}$  is the spin relaxation rate in the pumping (target) chamber. What makes the determination of  $X$  tricky is that we need to know its value before we can calculate  $u$  which is a prerequisite for  $X$ . However, because  $\delta\Gamma$  is such a small correction typically being 10% of less of the size of  $\Gamma_s$ , we solve this problem in an iterative manner.  $X$  is initially assumed to be 0 and plugged into Eq. 3.22, which in the end lead to a different value of  $X$  that is closer to its real value. After iterating this process a few times,  $X$  quickly converges to a stable value.

However, the hot relaxation method assumes the temperature dependence of the  $X$  factor is identical to the temperature dependence of  $\gamma_{se}$  by combining data taken at different temperature into one value of  $X$ . It is also time consuming to perform measurements shown in Fig. ???. For these two reasons, the hot relaxation method was only applied to a small number of cells.

In order to measure  $X$  factor at a single temperature and explore its temperature dependence, we used 4 four other methods to determine the value of  $X$  factor. All but the second method described below are based on the "polarization method" from Ref. [?]. The difference is that we used early time measurements of the initial spinups for  $P_A\langle\gamma_{se}\rangle$  for the third and fourth methods. And the second method is basically a single point measurement of the hot relaxation method described above.

We label the results from the four single temperature methods as  $X_1$ ,  $X_2$ ,  $X_3$  and  $X_4$  respectively. The most straightforward method requires measurements of  $\langle P_A \rangle$ ,  $P_{pc}^\infty$  and  $\Gamma_s$ . The equilibrium  $^3\text{He}$  polarization can be rewritten as

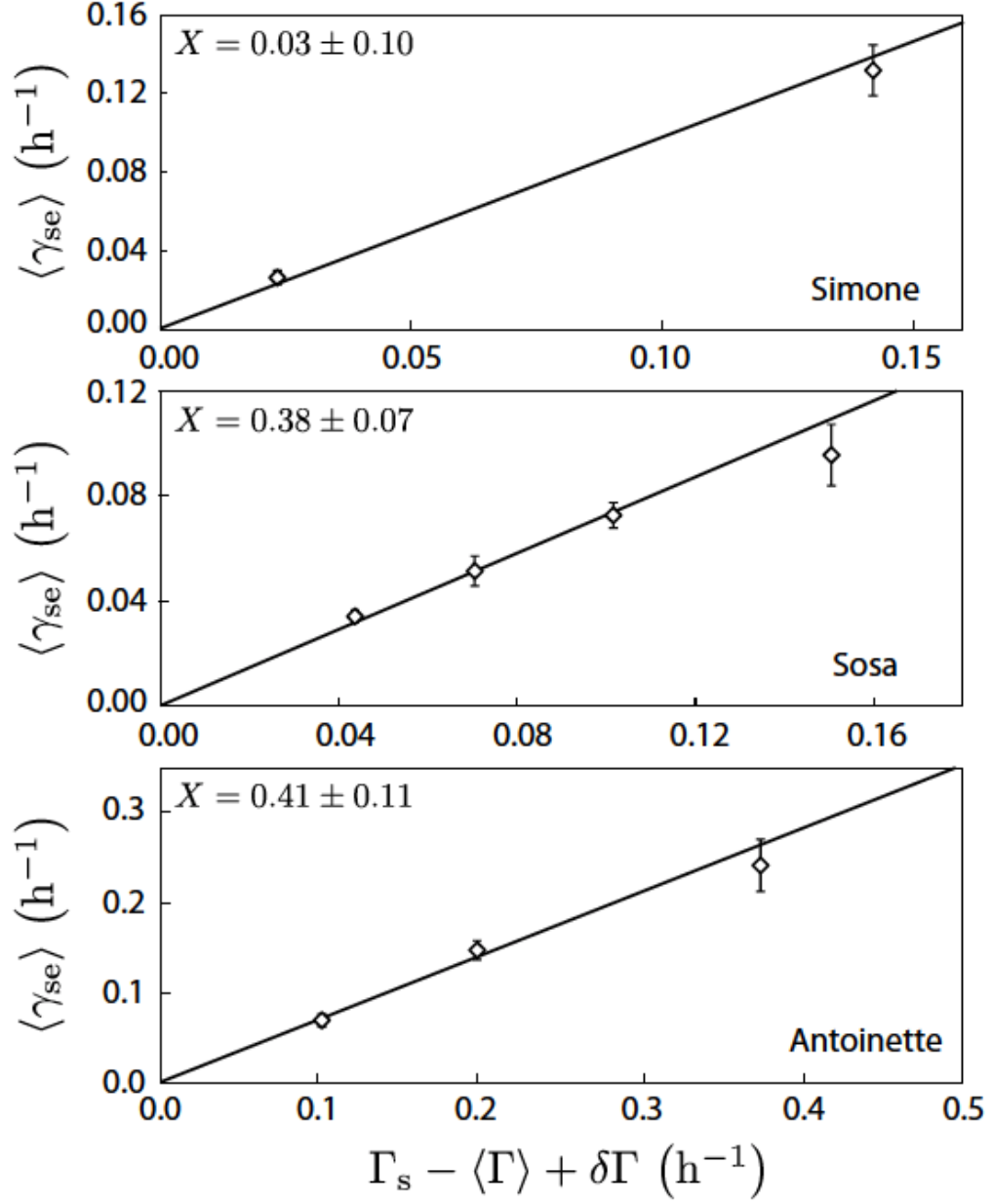


**Figure 3.6:** The cell-averaged spin-exchange rate  $\langle \gamma_{se} \rangle$  is calculated using data from Faraday rotation and the spin-exchange constants  $k_{se}^{Rb}$  and  $k_{se}^K$ . The three linear fits shown here are constrained to go through zero. The errors quoted in values of X factor include the uncertainty in our determination of  $k_{se}^K$ .

$$P_{pc}^{\infty} = \frac{\langle P_A \rangle \langle \gamma_{se} \rangle}{\Gamma_s + \delta\Gamma - \delta\Gamma'} \quad (3.23)$$

where  $\delta\Gamma' = f_{tc}\Gamma_{tc}^2/(\Gamma_{tc} + d_{tc})$ . Substitute Eq. 3.20 into Eq. 3.23,  $X_1$  is

$$X_1 = \frac{\langle P_A \rangle}{P_{pc}^{\infty}} \left( \frac{\Gamma_s - \langle \Gamma \rangle + \delta\Gamma}{\Gamma_s + \delta\Gamma - \delta\Gamma'} \right) - 1 \quad (3.24)$$

Just as what we did for the hot relaxation method, here  $\delta\Gamma$  is calculated in the same iterative manner.  $X$  is first taken as 0 and the iteration continued until  $X$  converged to a stable value.

For the second method, we first solve Eq. 3.20 for  $X$ :

$$X = \frac{\Gamma_s - \langle \Gamma \rangle + \delta\Gamma}{\langle \gamma_{se} \rangle} - 1 \quad (3.25)$$

then we substitute Eq. 3.15 into the equation above:

$$X_2 = \frac{\Gamma_s - \langle \Gamma \rangle + \delta\Gamma}{f_{pc}k_{se}^{Rb}[Rb](1 + D')} - 1 \quad (3.26)$$

Again  $\delta\Gamma$  is calculated iteratively. We chose to use our value of  $k_{se}^K$  for better consistency with the rest of our data.

The third method is very similar to the second, but we determine  $\langle \gamma_{se} \rangle$  with data from initial spinups:

$$\langle \gamma_{se} \rangle = f_{pc}m_{pc}^s / \langle P_A \rangle \quad (3.27)$$

Substitute the above equation into Eq. 3.25, we get

$$X_3 = \langle P_A \rangle \frac{\Gamma_s - \langle \Gamma \rangle + \delta\Gamma}{f_{pc}m_{pc}^s} - 1 \quad (3.28)$$



Note the quantity  $k_{se}^K$  used for  $X_2$  was obtained by fitting the ratio  $m_{pc}^F/m_{pc}^s$  to 1, thus for any hybrid cell,  $X_2$  and  $X_3$  are highly correlated. However, for pure Rb cell such as Sosa, these two methods are independent.

The fourth method is similar to the first one. It starts from Eq. 3.23, what makes it different from the first method is that it treats  $\langle\gamma_{se}\rangle$  as a known quantity and expresses  $\Gamma_s$  with it using Eq. 3.20, while the first method did it in the exact opposite way. Then the cell-averaged spin-exchange rate is evaluated with

$$\langle\gamma_{se}\rangle = f_{pc}m_{pc}^s/\langle P_A \rangle \quad (3.29)$$

Thus  $X_4$  is

$$X_4 = \frac{P_A}{P_{pc}^\infty} - \frac{\langle P_A \rangle (\langle \Gamma \rangle - \delta\Gamma')}{f_{pc}m_{pc}^s} - 1 \quad (3.30)$$

The computed X factors are shown in Table 3.3. The different values of X are quite consistent with each other. It is worth noting that even though  $X_1$  is completely independent of  $m_{pc}$  and  $k_{se}^K$ , it is still quite consistent with the rest of the X values. The last column in the table is a weighted average of either  $X_1$  and  $X_2$  ( $X_{12}$ ) or all four X values ( $X_{1234}$ ).

To the best of our knowledge, there has not been a dedicated study of the X factors and the their temperature dependence, with a large number of cells using measurements of the alkali polarization since the Babcock's *et al.* original work. Our results are an independent evidence of the existence of the X factor. According to our study, the X factor limits  $^3\text{He}$  polarization to 62-88% for the range of temperature we operate within.

Cell	T(°C)	$X_1$	$X_2$	$X_3$	$X_4$	$X_{12}/X_{1234}$
Simone	215	-0.02(12)	-0.10(14)	-	-	-0.04(12)
	255	0.13(08)	0.08(09)	-	-	0.11(06)
Sosa	160	0.22(07)	0.28(09)	0.32(15)	0.18(09)	0.24(06) <sup>†</sup>
	170	0.24(07)	0.37(15)	-	-	0.27(06)
	180	0.45(08)	0.40(09)	0.50(17)	0.45(09)	0.43(06) <sup>†</sup>
	190	0.59(16)	0.57(17)	-	-	0.58(12)
Boris	235	0.21(14)	0.31(14)	-	-	0.26(10)
Sam.	235	0.08(06)	0.22(09)	-	-	0.12(05)
Alex	235	0.34(09)	0.35(09)	0.63(20)	0.29(10)	0.34(06) <sup>†</sup>
Astral	235	0.15(07)	0.22(10)	0.20(14)	0.14(07)	0.17(05) <sup>†</sup>
Steph.	235	0.31(17)	0.31(10)	-	-	0.31(08)
Brady	235	0.13(07)	0.15(09)	0.23(14)	0.11(07)	0.14(05) <sup>†</sup>
Antoinette	215	0.27(09)	0.44(17)	0.30(19)	0.25(11)	0.28(08) <sup>†</sup>
	235	0.20(09)	0.34(12)	0.36(17)	0.15(09)	0.24(07) <sup>†</sup>
	255	0.55(26)	0.54(16)	0.50(30)	0.56(26)	0.55(13) <sup>†</sup>

**Table 3.3:** Shown are the values of the X factor at the indicated over set temperatures.

The last column is a weighted average of results from either the first two methods or all four methods. A <sup>†</sup> indicates combined values computed with all 4 methods.

# Bibliography

- [1] High-performance nuclear-polarized  $^3\text{He}$  targets for electron scattering based on spin-exchange optical pumping. *PhD thesis, University of Virginia*, 2010.
- [2] E. Babcock, I. A. Nelson, S. Kadlecik, and T. G. Walker.  $^3\text{He}$  polarization-dependent epr frequency shifts of alkali-metal- $^3\text{He}$  pairs. *Phys. Rev. A*, 71:013414, Jan 2005.
- [3] F. Bloch. Nuclear induction. *Phys. Rev.*, 70:460–474, Oct 1946.
- [4] G. D. Cates, S. R. Schaefer, and W. Happer. Relaxation of spins due to field inhomogeneities in gaseous samples at low magnetic fields and low pressures. *Phys. Rev. A*, 37:2877–2885, Apr 1988.
- [5] G. D. Cates, D. J. White, T.-R. Chien, S. R. Schaefer, and W. Happer. Spin relaxation in gases due to inhomogeneous static and oscillating magnetic fields. *Phys. Rev. A*, 38:5092–5106, Nov 1988.
- [6] E. M. M. V. Romalis and G. D. Cates. Pressure broadening of  $\text{Rb } d_1$  and  $d_2$  lines by  $^3\text{He}$ ,  $^4\text{He}$ ,  $\text{N}_2$ , and  $\text{Xe}$ : line cores and near wings. *Phys. Rev. A*, 56(6), 1997.

- [7] I. I. Rabi, N. F. Ramsey, and J. Schwinger. Use of rotating coordinates in magnetic resonance problems. *Rev. Mod. Phys.*, 26:167–171, Apr 1954.
- [8] M. L. R.Barbe and F. Laloe. Experimental verifications - measurement of the he3 self-diffusion coefficient. 35:935–951, 1974.
- [9] M. V. Romalis and G. D. Cates. Accurate  $^3\text{He}$  polarimetry using the rb zee-man frequency shift due to the Rb– $^3\text{He}$  spin-exchange collisions. *Phys. Rev. A*, 58:3004–3011, Oct 1998.
- [10] W. H. Thad G. Walker. Spin-exchange optical pumping of noble-gas nuclei. *RMP Colloquia*.

# Appendix A

## Appendix title

This is Appendix A.

You can have additional appendices too (*e.g.*, `apdxb.tex`, `apdxc.tex`, *etc.*). If you don't need any appendices, delete the appendix related lines from `thesis.tex` and the file names from `Makefile`.